Independent validation of IASI/METOP-A LMD and RAL CH_4 products using CAMS model, *in situ* profiles and ground-based FTIR measurements

Bart Dils[1], Minqiang Zhou[1,2], Claude Camy-Peyret[3,4], Martine De Mazière[1], Yannick Kangah[3], Bavo Langerock[1], Pascal Prunet[3], Carmine Serio[5], Richard Siddans[6], and Brian Kerridge[6]

[1]Royal Belgian Institute for Space Aeronomy (BIRA-IASB), Brussels, Belgium
[2]Institute of Atmospheric Physics, Chinese Academy of Sciences, Beijing, China
[3]SPAce SCIence Algorithmics (SPASCIA), Toulouse, France
[4]L'Institut Pierre-Simon-Laplace (IPSL), Paris, France
[5]UniversitA degli Studi della Basilicata (UniBas), Potenza, Italy
[6]STFC Rutherford Appleton Laboratory, Chilton, UK

Correspondence: Minqiang Zhou (minqiang.zhou@aeronomie.be)

Abstract. In this study, we carried out an independent validation of two methane retrieval algorithms using spectra from the Infrared Atmospheric Sounding Interferometer (IASI) onboard the Meteorological Operational satellite programme-A (MetOp-A) since 2006. Both algorithms, one developed by the Laboratoire de Météorologie Dynamique (LMD), called the non-linear inference scheme (NLISv8.3), the other by the Rutherford Appleton Laboratory (RAL), referred to as RALv2.0, provide long-term global CH_4 concentrations using distinctively different retrieval approaches (Neural Network vs. Optimal Estimation, respectively). They also differ with respect to the vertical range covered, where LMD provides mid-tropospheric dry air mole fractions (mtCH_4) and RAL provides mixing ratio profiles from which we can derive total column-averaged dry air mole fractions (XCH_4) and potentially 2 partial column layers (qCH_4).

We compared both CH_4 products using the Copernicus Atmospheric Monitoring Service (CAMS) model, *in situ* profiles (range extended using CAMS model data) and ground-based Fourier transform infrared (FTIR) remote sensing measurements. The average difference in mtCH_4 with respect to *in situ* profiles for LMD ranges between -0.3 and 10.9 ppb while for RAL the XCH_4 difference ranges between -10.2 and -4.6 ppb. The standard deviation (stdv) of the observed differences between *in situ* and RAL retrievals is 14.5-23.0 ppb, which is consistently smaller than that between *in situ* and LMD retrievals about 15.2-30.6 ppb. By comparing with ground-based FTIR sites, the mean difference is within ± 10 ppb for both RAL and LMD retrievals. However, the stdv of the differences at the ground-based FTIR stations show significantly lower values for RAL (11-16 ppb) than those for LMD (about 25 ppb).

The long-term stability and seasonal cycles of CH_4 derived from the LMD and RAL products are further investigated and discussed. The seasonal variation of XCH_4 derived from RAL is consistent with the seasonal variation observed by the ground-based FTIR measurements. However, the overall 2007-2015 XCH_4 trend derived from RAL measurements is underestimated if not adjusted for an anomaly occurring on 16 May 2013 due to a L1 calibration change. For LMD, we see very good

Atmospheric
Measurement
Techniques
Discussions

agreement at the (sub)tropics (<35°N-35°S), but notice deviations of the seasonal cycle (both in the amplitude and phase) and an underestimation of the long-term trend with respect to the RAL and reference data at higher latitude sites.

1   Introduction

Methane (CH_4) is an important greenhouse gas, which has a global warming potential about 28 times greater than carbon

5   dioxide (CO_2) over a 100-year time horizon (IPCC, 2013). As CH_4 has a relatively short lifetime of about 9 years as compared to CO_2, it is more efficient to control CH_4 emissions to mitigate climate change. About 60% of atmospheric CH_4 is released from fossil fuels, biomass burning, landfills and rice agriculture (anthropogenic activities) emissions, and the remaining 40% are coming from ruminant animals, termite, wetlands and lake (natural) emissions (IPCC, 2013). The major sink of CH_4 is its reaction with the hydroxyl radical (OH) to form CO_2 andh H_2O (Rigby et al., 2017).

10   The globally-averaged methane abundance measured by the NOAA marine surface sites shows that the dry air mole fraction of CH_4 increases from 1644.65 ppb in 1984 to 1772.41 ppb in 1999, and it keeps almost stable between 1999 and 2006. However, the CH_4 started increasing again (Rigby et al., 2008), from 1774.98 ppb in 2006 to 1911.82 ppb in 2022. Kirschke et al. (2013) showed that a rise in natural wetland and fossil fuel emissions accounts for the increase of CH_4 after 2006. CH_4 isotope measurements suggest that tropical biogenic sources are the cause of the increase (Schwietzke et al., 2016). Later,

15   Worden et al. (2017) pointed out that there is a decrease in the biomass burning emission after 2007, and the increases from fossil fuels and biogenic sources are both important. In addition to the emissions, the variation in OH can affect the CH_4 mole fraction, which might also contribute to the increase after 2007 (Turner et al., 2017).

The Infrared Atmospheric Sounding Interferometer (IASI) carried onboard the Meteorological Operational satellite programme-A (MetOp-A) was launched to a sun-synchronous orbit on October 19, 2006 and is recording infrared spectra in the wavenum-

20   ber range from 645 to 2760 cm^{-1} (Edwards et al., 2006). Since then, CH_4 has been successfully retrieved from the IASI observed spectra with several different algorithms, e.g. the Laboratoire de Météorologie Dynamique's (LMD) non-linear inference scheme (NLIS) (Crevoisier et al., 2009) and the Rutherford Appleton Laboratory (RAL) (Siddans et al., 2017). The LMD methane mid-tropospheric dry air mole fraction (mtCH$_4$) have been assimilated in the Copernicus Atmosphere Monitoring Service (CAMS) greenhouse gas model (Massart et al., 2014). Note that dry air mole fractions of methane are typically de-

25   noted as XCH$_4$ when they pertain to the total column. Therefore in the case of LMD, or when using LMD's vertical sensitivity profile for smoothing, mtCH$_4$ is often used as a better representation of its limited vertical range. In this article where we deal with comparisons between both total and partial column averaged mole fractions, we sometimes refer to mere CH_4, but note that, depending on the products this refers to differing dry air mole fractions be it XCH$_4$ (for total column RAL), qCH$_4$ (for RAL partial column) or mtCH$_4$ (for LMD or RAL smoothed by the LMD sensitivity profile, mid tropospheric partial columns).

30   RAL XCH$_4$ products are used for inverse modeling in order to optimize methane fluxes and to better understand the methane budget (Palmer et al., 2018). Crevoisier et al. (2013) compared the LMD data with aircraft measurements, and they found that the mean and standard deviation (stdv) of the differences are within 7.2 ppb and 16.3 ppb, respectively. Siddans et al. (2017) compared the RAL data with independent measurements from satellite, aircraft and ground sensors, and found that the

precision of a single retrieval ranges from 20 to 40 ppb, and the methane (XCH_4) trend between 2007 and 2012 derived from the RAL product is generally consistent with the CAMS model, but without quantitative result. As both RAL and LMD IASI MetOp-A retrievals provide long time series of CH_4 observations since 2007, the two products are valuable to study the CH_4 trend and variation on a global scale.

5   In this study, we make an independent validation of LMD and RAL CH_4 measurements from IASI/MetOp-A using CAMS model, aircraft and AirCore *in situ* profiles, and ground-based Fourier transform infrared (FTIR) measurements. The data used in this study are described in Section 2. The method of comparison between LMD and RAL measurements and the method of comparison between the satellite (both LMD and RAL) and reference data are discussed in Section 3. In Section 4, we show the results concerning the differences between the LMD and RAL CH_4 measurements, and the accuracy and precision of the

10   RAL and LMD IASI measurements. In Section 5, the annual growth and the seasonal variation of CH_4 dry air mole fractions derived from the RAL and LMD measurements are compared to each other as well as to the reference data. Discussions are carried out in Section 5 and conclusions are shown in Section 6.

2   Data

2.1   IASI satellite measurements

15   #### 2.1.1   RAL

The RAL retrieval algorithm is based on the optimal estimation method (OEM) as described in (Rodgers, 2000) using the Levenberg-Marquardt iterative method exploiting the IASI spectra from 1232.25 to 1288.00 cm^{-1}. The spectral range differs from the one from IASI LMD NILSv8.3 in order to capture channels that are more sensitive to near surface concentrations. The RAL retrievals are performed globally over land and sea, by night and day (9:30 am/pm local solar time). The retrieval scheme

20   provides retrieved products at the IASI Instantaneous Field Of View (IFOV) scale, selecting one of the 4 IFOVs within a given Field Of Regard (FOR) with the warmest brightness temperature (BT) at 950 cm^{-1}. The RAL retrieval scheme uses nitrous oxide (N_2O) spectral features in the interval to estimate effective cloud parameters (Siddans et al., 2017). The temperature, water vapour, and surface spectral emissivity are pre-retrieved from the Infrared Microwave Sounder (IMS) retrieval.

RAL data used in this study is v2.0, covering measurement from 1 June 2007 to 31 December 2017. RAL IASI level 2

25   product provides *a priori* and retrieved CH_4 profiles, *a priori* and retrieved column-averaged XCH_4 mole fractions, column averaging kernel, averaging kernel matrix and the surface pressure. The latitude-dependent *a priori* CH_4 profile is applied. The degree of freedom for signal (DOFs) is about 2.0 with two pieces of information characterized by the partial columns of 0-6 km and 6-12 km. Note that the RAL retrievals used in this study are filtered as suggested in the RAL Product User Guide (Knappett, 2019).

2.1.2 LMD

The IASI LMD NILS algorithm, henceforward referred to as LMD, is based on a multilayer-perceptron scheme (Crevoisier et al., 2009). 24 IASI channels selected within the range from 1270 cm^{-1} to 1350 cm^{-1} and 2 AMSU channels (6 and 8) are exploited to retrieve CH_4 integrated columns. LMD provides a vertical CH_4 weighting function to represent the vertical

5 sensitivity. This product is mainly sensitive to the mid-to-upper tropospheric methane covering the vertical range between 100 hPa and 500 hPa (Crevoisier et al., 2009, 2013). An *a priori* profile is not required in the LMD retrieval algorithm and retrievals are performed over land and sea, by night and day for clear-sky condition. Clouds are detected by multi-spectral threshold tests using AMSU and High resolution Infrared Radiation Sounder (HIRS)-4 brightness temperature differences together with a heterogeneity test at each HIRS FOV. Initially LMD NILS targeted tropical regions (30° N-30° S) only.

10 Currently the retrievals are performed globally, with the exception of polar situations. In this analysis, for general quality markers and direct comparisons with RAL, we limit ourselves to data coming from the 60° North-60° South latitude band as advised by the product development team.

The inference scheme uses an average of the 4 IASI footprints contained in each single AMSU FOV. Hence, retrievals are performed at the AMSU spatial resolution, roughly comparable with the IASI field of regard composed by 4 IASI IFOV. The

15 LMD data used in this study is v8.3 covering the measurement from 1 July 2007 to 29 September 2015. LMD IASI level 2 data provides a column-averaged mole fraction and weighting function. There is no profile provided by the LMD IASI mtCH$_4$ data.

2.2 *in situ* profiles

The geo-location of the *in situ* and ground-based FTIR measurements used in this study is shown in Figure 1.

20 ### 2.2.1 AirCore

The AirCore is an atmospheric sampling system that uses a long tube that is carried into the stratosphere using balloons. It samples the air from the surrounding atmosphere and preserves profiles of the trace gases of interest from the surface (a few hundred meters) to the middle stratosphere (about 30 km; (Karion et al., 2010)). The NOAA Global Monitoring Laboratory has carried out many AirCore launches during the last decade at selected sites (Boulder, Colorado; Lamont, Oklahoma; Lauder,

25 New Zealand; Sodankylä, Finland; Park Falls, Wisconsin and Edwards AFB/Dryden, California), and more recently has made further system improvements by developing active capabilities by mounting the AirCore system on aircrafts or UAV drones (Andersen et al., 2018). Here, we use the NOAA AirCore v20181101 profiles (Baier et al., 2021).

2.2.2 HIPPO

The HIAPER Pole-to-Pole Observations (HIPPO) are aircraft measurements (Wofsy, 2011), using an NSF/NCAR Gulfstream-

30 V, performed as Pole-to-Pole campaigns which occurred five times during the 2009-2011 time period. HIPPO transected the mid-Pacific ocean and returned either over the Eastern Pacific, or over the Western Atlantic, making frequent surface to

tropopause ascents and descents. The HIPPO data were collected in different seasons, and they have been widely applied for scientific studies. Since, unlike AirCore, its vertical range does not cover the entirety of the range to which the retrieval algorithms are sensitive, we need to expand the profiles using other data (in our case from the CAMS model) as outlined in section3.4.1).

2.2.3 IAGOS

In-service Aircraft for a Global Observing System (IAGOS) is a European Research Infrastructure for global observations of atmospheric composition from commercial aircraft. IAGOS combines the expertise of scientific institutions with the infrastructure of civil aviation in order to provide essential data on climate change and air quality at a global scale. It is composed of two complementary systems: (i) IAGOS-CORE providing global coverage on a day-to-day basis of key observables and (ii) IAGOS-CARIBIC providing a more in-depth and complex set of observations with lesser geographical and temporal coverage. In this study, we select all the IAGOS CARIBIC CH_4 profiles, measured during ascent or descent of the commercial aircraft from or towards its airport, between 10 July 2007 and 31 December 2017. As with the HIPPO data, profile extension prior to the comparisons is required.

2.3 Ground-based FTIR measurements

2.3.1 TCCON

The Total Carbon Column Observing Network (TCCON) is a network of ground-based FTIR that record spectra of the sun in the near-infrared. From these spectra, the CH_4 and O_2 total columns are retrieved simultaneously. The retrieved windows of CH_4 are 5781.0-5897.0, 5996.45-6007.55 and 6007.0-6145.0 cm^{-1}, and the retrieved window of O_2 is 7765-7905 cm^{-1}. Since the O_2 volume mixing ratio (VMR) of 0.2095 is constant in the atmosphere, TCCON uses the O_2 total column to calculate the total column of the dry air, and then to calculate the XCH_4 as the ratio between the retrieved CH_4 total column and the total column of dry air. The advantage is that systematic errors common to the retrieval of CH_4 and O_2 retrieval partially cancel in the calculation of the column average mole fractions resulting in a high precision data product. Furthermore TCCON applies a calibration factor to reduce its systematic bias (Wunch et al., 2011). Currently the TCCON network is going through a transition period, moving from the GGG2014 to the GGG2020 retrieval algorithm version. While most stations have already delivered GGG2020 data, for the time period we are analyzing, many gaps are still present in the new dataset, particularly older data still needs to be reprocessed. In stead of using a mixture of GGG2020 and GGG2014 data, we opted to use GGG2014 data exclusively. The random uncertainty of TCCON XCH_4 measurement is about 0.5 % (Wunch et al., 2015). The TCCON sites used in this study are listed in Table 1.

2.3.2 NDACC

The Network for the Detection of Atmospheric Composition Change (NDACC) hosts ground-based solar absorption FTIR measurements of CH_4 from mid-infrared spectra. NDACC uses either the SFIT4 or the PROFFIT9 algorithm to retrieve CH_4

Atmospheric
Measurement
Techniques

Open Access

Discussions

EGU

Table 1. Characteristics of the TCCON sites used in this study: location, altitude (in km a.s.l.) and reference.

Site	Latitude	Longitude	Altitude [km]	Reference
Eureka	80.05°N	86.42°W	0.61	Strong et al. (2019)
Sodankylä	67.37°N	26.63°E	0.19	Kivi et al. (2014)
Bialystok	53.23°N	23.05°E	0.18	Deutscher et al. (2019)
Bremen	53.10°N	8.85°E	0.03	Notholt et al. (2019)
Karlsruhe	49.10°N	8.44°E	0.12	Hase et al. (2015)
Orleans	47.97°N	2.11°E	0.13	Warneke et al. (2019)
Garmisch	47.48°N	11.06°E	0.74	Sussmann and Rettinger (2018)
ParkFalls	45.95°N	90.27°W	0.44	Wennberg et al. (2017)
Rikubetsu	43.46°N	143.77°E	0.38	Morino et al. (2018b)
Lamont	36.60°N	97.49°W	0.32	Wennberg et al. (2016b)
Tsukuba	36.05°N	140.12°E	0.03	Morino et al. (2018a)
Edwards	34.96°N	117.88°W	0.70	Iraci et al. (2016)
JPL	34.20°N	118.18°W	0.39	Wennberg et al. (2016a)
Pasadena	34.14°N	118.13°W	0.23	Wennberg et al. (2015)
Saga	33.24°N	130.29°E	0.01	Kawakami et al. (2014)
Izaña	28.30°N	16.50°W	2.37	Blumenstock et al. (2017)
Ascension	7.92°S	14.33°W	0.01	Feist et al. (2014)
Darwin	12.46°S	130.93°E	0.04	Griffith et al. (2014a)
Reunion	20.90°S	55.49°E	0.09	De Mazière et al. (2017)
Wollongong	34.41°S	150.88°E	0.03	Griffith et al. (2014b)
Lauder	45.04°S	169.68°E	0.37	Sherlock et al. (2014)

vertical profiles (De Mazière et al., 2018). Good agreement between these two retrieval algorithms has been demonstrated (Hase et al., 2004), and both algorithms are based on the optimal estimation method. The CH_4 retrieval strategy within the NDACC community has not been fully harmonized, but it uses the CH_4 absorption lines around 2800 cm^{-1} (3.57 μm). The DOFs is about 2.5, with about two pieces of information in the troposphere and in the stratosphere separately (Zhou et al.,

5   2018). The systematic and random uncertainties of NDACC CH_4 total column are estimated to be 3.0% and 1.5%, respectively. The estimated systematic uncertainty of 3.0% is mainly coming from the uncertainty of the spectroscopy. By comparing the TCCON and NDACC XCH_4 measurements, Ostler et al. (2014a) pointed out that there is no overall bias between TCCON and NDACC XCH_4 retrievals. Since the systematic uncertainty of TCCON measurement is largely eliminated by applying a scaling factor via the comparison to *in situ* profiles, we can assume that there is no overall bias in the NDACC network either. For

10   TCCON we can estimate the accuracy of this network from the uncertainty on the scaling factor, which amounts to 0.2%. The

Atmospheric
Measurement
Techniques
Discussions

NDACC data provide *a priori* and retrieved profiles, averaging kernel and the surface pressure. The NDACC sites used in this study are listed in Table 2.

Table 2. Characteristics of the NDACC sites used in this study: location and altitude (in km a.s.l.).

Site	Latitude	Longitude	Altitude [km]	PI
Eureka	80.05°N	86.42°W	0.61	K.Strong (U. of Toronto)
Thule	78.90°N	68.77°W	0.02	J.Hannigan, I. Ortega, M. Coffey (NCAR)
Kiruna	67.84°N	20.40°E	0.2	T. Blumenstock (IMK-ASF), U. Raffalski (IRF), Y. Matsumi (STEL)
St.Petersburg	59.88°N	29.83°E	0.02	M. Makarova (SPBU)
Garmisch	47.48°N	11.06°E	0.74	R.Sussmann (KIT-IFU)
Zugspitze	47.42°N	10.98°E	2.96	R.Sussmann (KIT-IFU)
Jungfraujoch	46.55°N	7.98°E	3.58	E. Mahieu (U. Liège)
Izaña	28.30°N	16.50°W	2.37	M. Schneider (KIT-IMK), O. Garcia (AEMET)
Mauna Loa	19.54°N	155.57°W	3.40	J. Hannigan, I. Ortega, M. Coffey (NCAR)
Reunion St-Denis	20.90°S	55.49°E	0.09	M. De Mazière (BIRA-IASB)
Reunion Maïdo	21.08°S	55.38°E	2.16	M. De Mazière (BIRA-IASB)
Wollongong	34.41°S	150.88°E	0.03	N. Jones, D. Griffith (U. Wollongong)
Lauder	45.04°S	169.68°E	0.37	D. Smale and J. Robinson (NIWA)

2.4 CAMS model

The reanalysis Copernicus Atmospheric Monitoring Service (CAMS) model, currently covers the 2003-2020 period. It comes
5   in the form of the standard reanalysis product in which satellite methane data is assimilated (including IASI LMD NILSv8.3, and thus cannot be regarded as an independent source for quality arbitration between the two algorithms in this study) or in the form of a control run without assimilation (Inness et al., 2019). The latter one, used here, constrains the meteorological parameters by observations while the methane field is free to evolve based on transport, fluxes and chemical loss rates (emission databases and loss rates described in (Massart et al., 2014). More information about the CAMS reanalysis greenhouse model is
10   available at https://confluence.ecmwf.int/display/CKB/CAMS%3A+Reanalysis+data+documentation (last access: 12 January 2023) and Agusti-Panareda et al. (2017).

The performance of the CAMS reanalysis XCH_4 control run in the 2003-2016 period has been validated using (among others) ground-based FTIR measurements (Ramonet et al., 2020), and it is found that the mean differences between the CAMS model and FTIR measurements are -0.7% in the troposphere and 3.6% in the stratosphere. The CAMS model can well capture
15   the long-term trend in XCH_4 between 2003 and 2016. For the column averaged mole fraction, the average biases at individual stations always remained below 20 ppb, with slightly higher CAMS values over mid and high latitudes and lower values in the tropics with respect to the FTIR measurements.

Atmospheric
Measurement
Techniques
Discussions
Open Access
EGU

3 Method

3.1 Smoothing RAL profile with LMD weighing function

To compare LMD with the RAL CH_4 measurements, we need to take the vertical sensitivity into account (Rodgers and Connor, 2003). Figure 2 shows the vertical sensitivities of both the LMD and RAL retrieved CH_4. While the LMD retrieval is mainly

5   sensitive to the mid to upper troposphere, RAL's sensitivity extends to lower altitudes.

For the LMD retrieval, the mtCH_4 product can be written:

$$c_{r,L} = \frac{\boldsymbol{wfdp} \cdot \boldsymbol{x_t}}{\sum \boldsymbol{wfdp}} = \boldsymbol{A_L} \cdot \boldsymbol{x_t} + \epsilon_L, \tag{1}$$

where $c_{r,L}$ is the retrieved LMD mtCH_4 and ϵ_L the retrieval errors without the smoothing effects, $\boldsymbol{wf}$ is the weighting function of the LMD retrieval interpolated on a pressure grid of thickness $\boldsymbol{dp}$, $\boldsymbol{x_t}$ is the true CH_4 profile, and $\boldsymbol{A_L}$ is the resulted

10   weighting function on the new grid.

For the RAL retrieval,

$$\boldsymbol{x_{r,R}} = \boldsymbol{x_a} + \mathbf{A_R}(\boldsymbol{x_t} - \boldsymbol{x_a}) + \epsilon_R, \tag{2}$$

where $\boldsymbol{x_{r,R}}$ and $\boldsymbol{x_a}$ are the retrieved and *a priori* CH_4 profiles, $\boldsymbol{A_R}$ is the averaging kernel matrix and ϵ_R the retrieval errors without the smoothing effects.

15   In this study, when we directly compare LMD to RAL, we calculated, from the RAL profile, the mid-tropospheric column-averaged mtCH_4, named RAL_LMDavk, using the LMD weighting function as follows:

$$\boldsymbol{x_{RAL\_LMDavk}} = \frac{\boldsymbol{wfdp} \cdot \boldsymbol{x_{r,R}}}{\sum \boldsymbol{wfdp}} \tag{3}$$

The vertical sensitivity of the RAL_LMDavk is also shown in Figure 2, which becomes much closer to that of the LMD retrieval. Then, the difference between LMD and RAL_LMDavk retrievals is mainly coming from the smoothing error of the

20   RAL retrieval smoothed with the vertical sensitivity of the LMD retrieval.

3.2 Comparison with the CAMS model

Prior to comparing RAL and LMD CH_4 with CAMS model data, all data, including averaging kernels and sensitivities, are averaged onto a $1° \times 1°$ latitude longitude grid. Satellite data is divided into day and nighttime data based on the solar zenith angle. We then construct a single daily daytime and nighttime CAMS global field by selecting from the standard 3 hourly output

25   those longitude bands that most closely correspond with the local IASI daytime (9:30 AM local solar time) and nighttime (9:30 PM) overpass times. Subsequently the daytime/nighttime model data is interpolated onto the satellite's vertical grid and smoothing is applied as per section 3.1. This allows for a straightforward comparison between the satellite and model global fields. In the case of comparisons with RAL_LMDavk, the CAMS data is first subject to smoothing using the RAL profile averaging kernel, after which we subsequently apply the LMD vertical sensitivity.

3.3 Co-located data pair between satellite and reference measurements

For each *in situ* profile (aircraft or AirCore), we use the same spatial-temporal criteria to select the co-located RAL and LMD satellite footprints. The IASI retrieved values (also called satellite measurements or satellite values for simplicity) are selected within a temporal window of ± 6 hours and a spatial distance within $\pm 1.0°$ latitude and $\pm 3.0°$ longitude. Then, the mean of

5   the satellite values is applied to compare with the *in situ* measurement.

For the ground-based FTIR measurement, we also use the mean of the co-located satellite measurements to compare with each individual FTIR measurement. Several spatial-temporal criteria have been tested and the following spatial-temporal criteria are finally set to select the co-located satellite footprints. Note that the criteria are different with TCCON or NDACC and LMD or RAL, which is mainly due to the different data densities of both ground-based FTIR and satellite measurements.

10   – RAL vs TCCON

       Co-located criteria: ± 1 hour and within a $\pm 0.5°$ latitude and $\pm 1.5°$ longitude

     – RAL vs NDACC

       Co-located criteria: ± 3 hours and within a $\pm 0.5°$ latitude and $\pm 1.5°$ longitude

     – LMD vs TCCON

15   Co-located criteria: ± 1 hour and within a $\pm 1.0°$ latitude and $\pm 3.0°$ longitude

     – LMD vs NDACC

       Co-located criteria: ± 3 hours and within a $\pm 1.0°$ latitude and $\pm 3.0°$ longitude

3.4 Comparison with reference data

3.4.1 Satellite vs *in situ* measurements

20   According to (Rodgers and Connor, 2003), the vertical sensitivity of the remote sensing data should be taken into account when comparing to *in situ* profile. To that end, we need to extrapolate the *in situ* profile to the whole atmosphere, as the vertical coverage of the *in situ* profile (IAGOS, HIPPO, and to a lesser extent AirCore) is limited. In this study, we use the CAMS model to extend the *in situ* profile. For the vertical range above the maximum height of the *in situ* data, we use the CAMS model profile but scaled with altitude-dependent factors. The scaling factor is equal to 1 at the top of the atmosphere, and to

25   the mean ratio of the CAMS model to the *in situ* measurements at the highest 3 levels where the CAMS profile meets up with the top of the measured profile. A linear fitting is applied to create the scaling factors between the maximum height of the *in situ* profile and the top of the atmosphere. For the vertical range below the minimum height of the *in situ* profile, the CAMS model with a constant offset is used. The offset is calculated as the mean difference between the CAMS model and *in situ* data in the lowest 3 levels. Of the 3 datasets, only AirCore measures well into the stratosphere, capturing the sharp CH_4 decreases

30   as one goes from the troposphere into the stratosphere. Therefore any observed differences between the validation results are at least in part due to inaccuracies within the extrapolated scaled model part of the *(*in situ*)* profiles. Other factors are differing

Atmospheric
Measurement
Techniques
Discussions

Open Access

EGU

geographical coverages, with HIPPO covering the Pacific region, IAGOS restricted to a handful of international airports and AirCore limited to a few sites in the United States and Sodankyla in Finland (see Figure 1).

-> RAL against *in situ* profile

The smoothed XCH$_4$ *in situ* measurement c_i is calculated as follows:

$$c_i = c_a + \boldsymbol{a_S}(\boldsymbol{x_i} - \boldsymbol{x_a}), \tag{4}$$

where $\boldsymbol{a_S}$ is the RAL column averaging kernel vector, $\boldsymbol{x_a}$ and $\boldsymbol{x_i}$ are the RAL *a priori* profile and *in situ* profile, respectively; c_a is the RAL IASI *a priori* XCH$_4$

For profile comparison, we also calculate the smoothed CH$_4$ profile *in situ* measurement $\boldsymbol{x_i}'$ as follows:

$$\boldsymbol{x_i}' = \boldsymbol{x_a} + \mathbf{A_R}(\boldsymbol{x_i} - \boldsymbol{x_a}), \tag{5}$$

using RAL's $\boldsymbol{A_R}$ averaging kernel matrix.

-> LMD against *in situ* profile

LMD IASI data only provides mtCH$_4$ together with the weighting function. There is no information about the *a priori* profile and the surface pressure.

$$c_i = \frac{\boldsymbol{wfdp} \cdot \boldsymbol{x_i}}{\sum \boldsymbol{wfdp}}, \tag{6}$$

3.4.2 Satellite vs FTIR measurements

When comparing the satellite and ground-based FTIR measurements, we need to take both the *a priori* profile and vertical sensitivity into account.

-> RAL against TCCON measurements

TCCON and RAL IASI data both provide their respective *a priori* profiles. Here, we use the TCCON *a priori* profile as the common *a priori* profile to adapt the RAL IASI data.

$$c'_{r,R} = c_{r,R} + c_{a,T} - c_{a,R} + \boldsymbol{a_S}(\boldsymbol{x_{a,R}} - \boldsymbol{x_{a,T}}), \tag{7}$$

where $c_{r,R}$ is the original RAL XCH$_4$ data, $\boldsymbol{a_S}$ is the RAL column averaging kernel vector, $\boldsymbol{x_{a,R}}$ and $\boldsymbol{x_{a,T}}$ are the RAL and TCCON *a priori* profiles, $c_{a,R}$ and $c_{a,T}$ are the RAL and TCCON *a priori* XCH$_4$, respectively.

To take the vertical sensitivity of the RAL retrieval into account, we apply the smoothing correction on the retrieved FTIR profile. However, TCCON only delivers a total column-averaged mole fraction and no retrieved profile on which we could apply our sensitivity corrections. This is due to the fact that TCCON performs a scaling profile retrieval allowing for no variation in the profile shape. In this study, we calculate the ratio of the TCCON retrieved XCH$_4$ ($c_{r,T}$)

Atmospheric
Measurement
Techniques
Open Access
EGU
Discussions

to the *a priori* XCH$_4$ ($c_{a,T}$), and the ratio is then multiplied by the TCCON *a priori* profile $\boldsymbol{x_{a,T}}$ as the retrieved TCCON profile ($\boldsymbol{x_{r,T}}$). After that, we apply the smoothing correction using the RAL IASI column averaging kernel

$$c'_{r,T} = c_{a,T} + \boldsymbol{a_S}(\boldsymbol{x_{r,T}} - \boldsymbol{x_{a,T}}), \tag{8}$$

where $c'_{r,T}$ is the adapted TCCON XCH$_4$. The $\boldsymbol{x_{r,T}}$ is re-gridded to the RAL retrieval grid, so that the $c'_{r,T}$ and $c'_{r,R}$ have been computed on the same vertical layers. Here, we compare $c'_{r,T}$ with $c'_{r,R}$.

-> RAL against NDACC measurements

NDACC and RAL IASI data both provide the *a priori* profiles, and we apply the NDACC *a priori* profile as the common *a priori* profile to adapt the RAL IASI retrieved CH$_4$ profile

$$c''_{r,R} = c_{r,R} + c_{a,N} - c_{a,R} + \boldsymbol{a_S}(\boldsymbol{x_{a,R}} - \boldsymbol{x_{a,N}}), \tag{9}$$

where $c_{a,N}$ is the NDACC *a priori* XCH$_4$ and $\boldsymbol{x_{a,N}}$ is the NDACC *a priori* CH$_4$ profile. The retrieved NDACC CH$_4$ profile ($\boldsymbol{x_{r,N}}$) is smoothed with the RAL IASI column averaging kernel to consider the vertical sensitivity of the RAL IASI data.

$$c'_{r,N} = c_{a,N} + \boldsymbol{a_S}(\boldsymbol{x_{r,N}} - \boldsymbol{x_{a,N}}), \tag{10}$$

where $c'_{r,N}$ is the adapted NDACC XCH$_4$. The $\boldsymbol{x_{r,N}}$ is re-gridded to the RAL retrieval grid, so that the $c'_{r,N}$ and $c''_{r,R}$ have the same vertical ranges.

Here, we compare $c'_{r,N}$ with $c''_{r,R}$.

-> LMD against TCCON measurements

LMD IASI data only provides mtCH$_4$ together with the weighting function. LMD does not provide an *a priori* profile, so that it is not possible to apply *a priori* substitution.

The LMD weighting function is thus directly applied onto the scaled TCCON *a priori* profile, which is used as a proxy for a TCCON retrieved profile. By doing this, we can not only include the vertical sensitivity of the LMD retrieval, but also reduce the uncertainty resulting from the TCCON near surface profile shape since the LMD weighting function is equal to 0 in the lower troposphere.

$$c''_{r,T} = \frac{\boldsymbol{wfdp} \cdot \boldsymbol{x_{r,T}}}{\sum \boldsymbol{wfdp}}, \tag{11}$$

Here, we compare the LMD data $c''_{r,T}$ with $c_{r,L}$.

-> LMD against NDACC measurements

We applied the LMD IASI weighting function onto the retrieved NDACC CH$_4$ profile.

$$c''_{r,N} = \frac{\boldsymbol{wfdp} \cdot \boldsymbol{x_{r,N}}}{\sum \boldsymbol{wfdp}}, \tag{12}$$

Here, we compare the LMD data $c''_{r,N}$ with $c_{r,L}$.

3.5 Measurement uncertainty

The uncertainty of each *in situ* profile is carefully estimated. For the vertical range within the *in situ* measurements, the uncertainty is from the reported measurements, with 1.3 ppb for IAGOS data (Filges et al., 2015), 1.5 ppb for AirCore data (Karion et al., 2010) and 1.5 ppb for HIPPO data (Wunch et al., 2010). For the vertical range above the *in situ* measurements,
5   we use the difference between the model and the scaled model as the uncertainty. For the vertical range below the *in situ* measurements, the mean difference between the model and *in situ* measurement in the troposphere (below $\sim$150 hPa) is used as the uncertainty.

The combined uncertainty from satellite and *in situ* measurements is calculated as

$$\sigma_c = \sqrt{\sigma_{sat}^2 + \sigma_i^2}, \tag{13}$$

10   where σ_{sat} is the uncertainty of satellite data, and σ_i is the uncertainty of the *in situ* measurements. For the RAL measurement, the uncertainty is reported in the public data (about 35 ppb). For the LMD measurement, since there is no uncertainty value available, the stdv of the co-located satellite data is used as the uncertainty. Note that we only select the FTIR and satellite data pair, with more than 2 co-located satellite footprints.

3.6 Trend and seasonal variation

15   In this study, we derive the trend and seasonal variation of CH_4 between 1 July 2007 and 30 June 2015 (8 full years) from LMD and RAL measurements. We limit ourselves to this period to make the two satellite datasets have the same time coverage. According to the NOAA surface measurements (Dlugokencky et al., 1994), the global CH_4 mean concentration kept increasing between July 2007 and June 2015, with an annual growth rate of 6.9$\pm$0.6 ppb/yr (WMO, 2017).

The level 2 satellite data are binned into $1°\times1°$ grids to generate the level 3 daily means. The monthly data are created based
20   on the daily data, and then the long-term trends and seasonal variations are calculated from the monthly means at each grid. To derive the trends from the month means $Y(t)$, with t the time in a fractional year, we use a regression model that includes a periodic function to describe the seasonal cycle:

$$Y(t) = A_0 + A_1 t + \sum_{k=1}^{3}(A_{2k}\cos(2k\pi t) + A_{2k+1}\sin(2k\pi t)), \tag{14}$$

where t is in fraction of year, A0 is the intercept, A1 is the annual trend and A_2 to A_7 are the periodic amplitudes. Then, the
25   de-trended data ($Y(t)_d$) is calculated as

$$Y(t)_d = Y(t) - (A_0 + A_1 \cdot t). \tag{15}$$

The seasonal variation is represented by the monthly means of the de-trended data and their associated uncertainty (2σ).

4 Accuracy and precision

4.1 Internal consistency

Prior to our comparisons with reference data, we looked at several parameters within each of the datasets. In particular we were interested in day-night, scan angle, residual cloud cover and pixel to pixel (the latter two for RAL only as this information is

5 not present in the LMD product) differences. This was done by drawing up histogram plots and looking at the distribution of the global data (not shown here) for the 2014 October month.

For $mtCH_4$ LMD we observed very small day-night differences in the distribution over land with a slightly lower mean (~4 ppb) for daytime data compared to night-time data. Also, $mtCH_4$ values are slightly higher (~7 ppb) for the edge viewing angles than for the nadir pixels.

10 For XCH_4 RAL we observe slight day-night differences (within 5 ppb), in the averaged distribution. The day uncertainties (typical stdv of ~15-20 ppb) are, as expected, lower than night uncertainties (typical stdv of ~35-40 ppb). Also its nadir values are higher (up to 11 ppb) than its edge viewing angle data on the monthly and global mean XCH_4 especially over sea. Also, the nadir pixels exhibit lower retrieval uncertainties (~5 ppb over land/day on the median of the global distributions). Concerning the inter-pixel differences, the highest differences are observed for daytime XCH_4 and between pixel 3 and pixel

15 1 with averaged differences of about 7 ppb over land and 8 ppb over sea. The interpixel retrieval uncertainties are all within 3 ppb. This difference is unexpectedly large and is discussed further in Section 6.1. Also, filtering with IASI L2 cloud fraction had a slight impact (about 3 ppb on average) on the global distribution for the XCH_4. There is a slight decrease of the retrieval errors of about 2 ppb on averaged for cloud fraction <15%. All this indicates that the RAL cloud filtering condition already eliminates most of could affected scenes.

20 The above analysis does not exclude stronger differences on a regional scale. For instance strong negative day-night (with higher nighttime values) differences can be observed over desert regions (see Figure 3) in both LMD and RAL. Surface emissivity is difficult to handle in some areas of the Sahara where it is particularly low. This typically causes a negative difference, which is larger in day than night due to the high surface-air temperature contrast. Likewise high surface-air temperature contrasts can trigger the elevation of surface emissions and can thus induce a positive day-night difference. Note that all biases

25 are present with differences in seasonal variations and in various regions, and spectral and angular dependencies vary between different land types and surface topologies, respectively, in different areas.

4.2 Direct intercomparison

In order to directly compare RAL with LMD retrievals we need to consider some inherent differences between the satellite products first. Foremost, and already discussed, are the differing sensitivities as a function of altitude. Another source of differ-

30 ences is that RAL selects the best IFOV among the 4 of them within any given IASI FOR, whereas LMD uses a combination thereof, so a direct comparison on a measurement by measurement basis is impossible. Instead we opted to use the CAMS model as an intermediate. Not only can we compare the gridded satellite products to the model and to one another, but we can

also compare their respective biases towards the model. Doing so overcomes to a great extent the fact that, even when looking at the bias between LMD and RAL_LMDavk mtCH$_4$, differences in vertical sensitivity remain.

Figure 4 shows the monthly mean global bias (for January, April, July and October 2012) between the satellite products and the CAMS model, whereby the model is always smoothed with the respective sensitivity/averaging kernel profile. This is done

5   for both LMD (top row), RAL (second row) and RAL smoothed by the LMD sensitivity profile (third row). As one can see all products have their distinct regional and seasonal biases with respect to CAMS. All products seem to feature stronger biases at high latitudes, with LMD featuring particularly strong negative biases around the month of October in the Northern Boreal regions and RAL (total column and LMD smoothed) featuring strong positive values compared to CAMS (particularly over Northern latitudes in April and over Antarctica in January, RAL inland Greenland being a curious exemption to this pattern).

10 To limit the impact of these regions, the overall monthly mean biases as shown in the figure are drawn up from all values within 60° North and South, in line with LMD's recommended latitude range. We also found a few cases in which the application of the RAL column averaging kernel onto the CAMS profile yielded clear erroneous outliers. These have been filtered out using a interquartile-distance filter. No more that 5 pixels needed to be removed for each month. Looking at the thus obtained values we see that the RAL column averaged product features the lowest bias with respect to CAMS, and with lower scatter than

15 LMD. The overall bias between RAL_LMDavk and CAMS on the other hand is very similar to that of LMD-CAMS. Its scatter (stdv of the SAT-CAMS differences) is similar to total column RAL.

The bottom two rows in Figure 4 feature the comparison between LMD and RAL_LMDavk (4th row) and finally the difference in the respective biases of LMD and RAL_LMDavk with respect to CAMS (bottom row). This last comparison should, in theory, have minimized most of the residual sensitivity differences between both products and is thus the most

20 accurate representation of their respective overall differences. The direct comparison between LMD and RAL_LMDavk (4th row) still yields overall negative bias values in excess of -10 ppb. This disappears to a large extent when looking at their respective biases towards CAMS (bottom row), indicating that, even when smoothing RAL with the LMD sensitivity profile, their inherent sensitivity differences remain substantial. This observation is important when interpreting further comparison results. Also, while the average bias is small, we can still observe significant regional and seasonal biases between the products.

25 To highlight just a few areas, in January we observe large positive LMD-RAL bias values over the Pacific between 10°N and 30°N as well as more moderate positive biases over the entire Northern Hemisphere Atlantic Ocean and Western Europe. Strong negative biases are observed over the Canadian Boreal forests. The latter biases disappear in April, while the positive biases over the ocean become less outspoken. Strong positive biases are now observed over Eastern Europe. In June, the previous 20°N oceanic positive bias belt relocates to the Southern Hemisphere, while over land strong positive biases are

30 observed in Northern Egypt, East of the Caspian Sea, and the Central and Eastern United States. Strong negative biases occur over Indonesia and the Northern Pacific. In October a positive latitudinal bias belt between 10°S and 30°S can be observed over land and sea, while outspoken negative biases are visible at high Northern latitudes, although note that the most significant biases occur at >60°N, outside the LMD domain.

4.3 RAL vs *in situ* profiles

In this section, both the total column and two partial columns are compared to the *in situ* profiles. The latter is possible as the degrees of freedom (DOFs) of the RAL CH_4 profile is about 2.0, with two distinct pieces of information in partial columns of 0-6 km and 6-12 km.

4.3.1 Total column

The RAL and HIPPO XCH_4 together with their differences along with the latitude are shown in Figure 5. Both RAL and HIPPO measurements observe high XCH_4 in the Northern Hemisphere and low XCH_4 in the Southern Hemisphere. Specifically, the XCH_4 at 40°N is about 80 ppb larger than that at 40°S. Two XCH_4 peaks at about 35°N and 75°N are captured by both datasets. Only 49 out of 466 (10.5%) differences between HIPPO and RAL measurements are outside their combined 1 σ uncertainties. However, the mean of HIPPO measurements is 16.5 ppb larger than the mean of RAL measurements between 15°N and 15°S, with many differences beyond the combined uncertainties. The overall mean and stdv of the differences between HIPPO and RAL measurements are -4.6 ppb and 16.5 ppb, respectively. The scatter plot between HIPPO and RAL measurements shows that the correlation efficiency (R) is 0.84, indicating there is a good agreement between HIPPO and RAL measurements. The linear fit suggests that the RAL data is slightly less/greater than the HIPPO measurements when the XCH_4 is low/high.

Furthermore, the RAL XCH_4 are also compared to IAGOS and AirCore (not shown here). The mean and stdv of the differences between IAGOS and RAL measurements are -4.8 ppb and 23.0 ppb, respectively. The R between the IAGOS and RAL measurements is 0.46. 216 out of 260 differences between IAGOS and RAL measurements are within their combined 1 σ uncertainties. The mean and stdv of the differences between AirCore and RAL measurements are -10.2 ppb and 14.5 ppb, respectively. The R between AirCore and RAL measurements is 0.82 and the linear fit is close to the one-by-one line, indicating there is a good agreement between AirCore and RAL measurements. Indeed 40 out of 49 differences between AirCore and RAL measurements are within their combined uncertainties.

4.3.2 Partial columns

Figure 6 shows the RAL and HIPPO XCH_4 together with their differences along with the latitude in the vertical ranges of 0-6 km and 6-12 km. Again we have to note that the HIPPO and IAGOS aircraft profiles used, have been expanded with scaled CAMS model data. The mean and stdv of the differences between HIPPO and RAL measurements in the 0-6 km layer are -12.2 ppb and 26.5 ppb, respectively. The mean and stdv of the differences between HIPPO and RAL measurements in the 6-12 km layer are -1.6 ppb and 22.2 ppb, respectively. The R between HIPPO and RAL measurements are 0.87 and 0.76 in the 0-6 km and 6-12 km layers. XCH_4 generally increases with latitude in the Northern Hemisphere in the vertical range of 0-6 km, while there are two peaks in XCH_4 around 35°N and 75°N in the vertical range of 6-12 km. The HIPPO measurements are larger than the RAL data in 0-6 km layer. For this layer 325 out of 466 differences between HIPPO and RAL measurements are within their combined uncertainties, and the underestimation of RAL measurements is particularly found in the tropical region. For the 6-12 km layer, 343 out of 466 differences between HIPPO and RAL measurements are within their combined

uncertainties, and the RAL and HIPPO measurements are close to each other in the tropical region. The stdv of the differences between RAL and HIPPO measurements in both partial columns are larger than that in the total column, reflecting that the uncertainties of the partial columns (0-6 km and 6-12 km) are larger than that of the total column.

The mean and stdv of the differences between IAGOS and RAL measurements in the 0-6 km layer are -9.5 ppb and 36.0 ppb, respectively. The mean and stdv of the differences between IAGOS and RAL measurements in the 6-12 km layer are -4.9 ppb and 23.2 ppb, respectively. The R between IAGOS and RAL measurements are 0.58 and 0.51 in the 0-6 km and 6-12 km layers. For the lower layer (0-6 km), 171 out of 260 differences between IAGOS and RAL measurements are within their combined uncertainties. For the upper layer (6-12 km), 150 out of 260 differences between IAGOS and RAL measurements are within their combined uncertainties. The mean and stdv of the differences between AirCore and RAL measurements in 0-6 km are -22.5 ppb and 27.1 ppb, respectively. The mean and stdv of the differences between AirCore and RAL measurements in the 6-12 km layer are -10.6 ppb and 26.1 ppb, respectively. The R are 0.75 and 0.51 in the 0-6 km and 6-12 km layers. For the lower layer (0-6 km), 31 out of 49 differences between AirCore and RAL measurements are within their combined uncertainties in 0-6 km. Only 20 out of 49 differences between AirCore and RAL measurements are within their combined uncertainties in 6-12 km. The standard deviation and R results for IAGOS are markedly worse than for HIPPO and AirCore.

4.4 LMD vs *in situ* profiles

Figure 7 shows the LMD and HIPPO mtCH$_4$ together with their differences along with the latitude. The data density of the LMD data is much less than the RAL data, but co-located LMD measurements are still able to observe the high mtCH$_4$ in the Northern Hemisphere and the low mtCH$_4$ in the Southern Hemisphere as expected. LMD nicely captures the overall latitudinal distribution of CH$_4$ with no obvious issues. As already mentioned in Section 3.4, the stdv of the co-located LMD measurements are calculated as the retrieval uncertainty of the LMD data because of no reported uncertainty. As a result, 34 out of 97 differences between HIPPO and LMD measurements are within their combined uncertainties. The mean and stdv of the differences between HIPPO and LMD measurements are -10.9 ppb and 27.7 ppb, respectively. The R between HIPPO and LMD measurements is 0.48.

Similarly, the IAGOS and AirCore measurements are used to compare with co-located LMD data. The mean and stdv of the differences between IAGOS and LMD measurements are 2.3 ppb and 30.6 ppb, respectively. The R between IAGOS and LMD measurements is 0.49. Only 27 out of 58 differences between IAGOS and LMD measurements are within their combined uncertainties. Only 3 co-located LMD and AirCore are selected, and 2 out of 3 differences between AirCore and LMD measurements are within their combined uncertainties. The mean and stdv of the differences between AirCore and LMD measurements are -0.3 ppb and 15.2 ppb, respectively. The R between AirCore and LMD measurements is 0.60.

4.5 RAL vs ground-based FTIR measurements

As the ground-based FTIR measurements (both TCCON and NDACC) have limited vertical information in the troposphere, we only focus on the total column of RAL in this section. Figure 8 shows the time series of the differences between the TCCON and RAL IASI 2-weekly means at 21 sites between July 2007 and June 2015. The sites are sorted by their latitudes from

north to south. The absolute mean and stdv of the differences (SAT-GB) at all sites are 4.31 ppb and 6.13 ppb, respectively. The differences are within $\pm$ 20 ppb, and there is no clear seasonal variation in the differences at most sites. For high-latitude sites (Eureka and Sodankylä), the RAL XCH_4 is larger than the TCCON measurements, especially in spring. Ostler et al. (2014b) pointed out that the smoothing error of TCCON XCH_4 retrieval is large under the polar vortex situation, and the

5   TCCON measurement is about 40 ppb larger than the real status. However, we find that the RAL XCH_4 is even larger than the TCCON measurement in spring at high-latitude sites. The time series of the differences between the NDACC and RAL IASI measurements at 13 sites are also shown in Figure 8. The mean and stdv of the differences are 9.55 ppb and 12.03 ppb, respectively. Similar to the TCCON comparison, for the low- and mid-latitude sites, it is found that there is no latitude dependence in the difference between RAL and NDACC measurements, and the differences are within $\pm$20 ppb. However, in

10   high-latitude sites (>60°N) the RAL XCH_4 is 20-100 ppb systematically larger than the NDACC measurements at Tule, and the RAL XCH_4 is generally larger than the NDACC measurements in winter at Kiruna. Also for TCCON, the Sodankyla and Eureka sites feature a stronger (>10 ppb) bias compared to the other stations. Moreover this stronger bias is most prominent in winter.

4.6   LMD vs ground-based FTIR measurements

15   Figure 9 shows the time series of the differences between the ground-based FTIR and LMD IASI measurements between July 2007 and June 2015. Compared to RAL measurements, there are no available co-located LMD measurements at Eureka, Rikubestu and Edwards TCCON sites. The mean and stdv of the differences are -4.76 ppb and 16.32 ppb, respectively. It is noticed that the mean differences vary with latitude, with positive values in the tropical and high-latitude regions, but negative values in the mid-latitude region. Moreover, there is a strong seasonal variation in the difference. For example, at Lamont,

20   the LMD IASI is about 20 ppb larger than the TCCON measurement in summer but it is about 60 ppb less than the TCCON measurement in winter. The mean and stdv of the differences between LMD and NDACC measurements are 2.83 ppb and 18.54 ppb, respectively. Similar to the TCCON measurements, the dependencies of the differences on latitude and time are also observed by the NDACC measurements.

4.7   Short summary

25   In this section we looked at internal consistency (particularly day-night differences as well as inter-pixel biases (the latter for RAL only). We also used CAMS as an intermediate to directly compare the RAL and LMD products revealing that, while the overall bias is small, significant regional and seasonal biases exists between the two and that applying the LMD averaging kernel onto the RAL product alone still incurs over a -10 ppb LMD-RAL overall bias. We also used aircraft (HIPPO and IAGOS) and AirCore *in situ* profiles to compare with two IASI CH_4 products from RAL and LMD. The mean and stdv of

30   the differences, together with the R and N (the number of measurement pairs) are summarized in Table 3. More than 80% of the differences between *in situ* and RAL XCH_4 measurements are within their combined uncertainties, and about 50% of the differences between *in situ* and LMD $mtCH_4$ measurements are within their combined 1 σ uncertainties (where thus 68% is expected). Of the 3 *in situ* measurement data used, AirCore, which measures profiles well into the stratosphere, can

Atmospheric
Measurement
Techniques
Open Access
Discussions
EGU

be considered the most representative. Unfortunately while the LMD-AirCore bias is lower than that of RAL, its very limited dataset does not warrant a definitive conclusion. Looking closer at the HIPPO measurements we see that the biases with respect to HIPPO are far more outspoken in the LMD data, as compared to RAL. Note that HIPPO measurements are concentrated around the Pacific Ocean area (Figure 1) and thus do not yield a global picture of the quality. Here we observe that the more

5   outspoken bias outliers in Figure 7 spatially and temporally correspond closely with the outliers as observed between CAMS and LMD (Figure 4 top row). RAL-CAMS biases (Figure 4 second row) in this area are not as strong which is again reflected in the HIPPO comparisons. The IAGOS measurements on the other hand, due to their irregular and often limited spatial and temporal distribution combined with inherent scatter didn't allow us to determine whether the observed RAL-LMD differences (Figure 4 bottom row) can be attributed to either algorithm. It is also very important to note that both HIPPO and IAGOS

10   need extending the aircraft *in situ* profiles with CAMS model data. Particularly potential model errors in the exact location of the sharp CH_4 concentration decrease as one ascends through the Upper Troposphere-Lower Stratosphere (UTLS) can have a significant impact which is hard to quantify with no exact information on the true state of the atmosphere. Therefore HIPPO's corroboration of the CAMS comparison results should be interpreted with extreme caution. As a test we artificially lowered or heightened the point at which the UTLS CH_4 CAMS transition kicks in by 100 hPa. This nullified most but not all of the most outspoken biases between LMD and HIPPO.

Table 3. The mean and stdv of the difference between *in situ* and IASI satellite CH_4 measurements.

in situ	IAGOS		AirCore		HIPPO	
Satellite	LMD	RAL	LMD	RAL	LMD	RAL
mean (SAT-AIR) [ppb]	2.3	-4.8	-0.3	-10.2	10.9	-4.6
stdv (SAT-AIR) [ppb]	30.6	23.0	15.2	14.5	27.7	16.5
R	0.49	0.46	0.60	0.82	0.48	0.84
N	58	260	3	49	97	466

15

For RAL data, the uncertainties of the retrieved partial columns (0-6 km and 6-12 km) are also validated by comparing them to the *in situ* profiles (Table 4). In general, the mean and stdv of the difference between the *in situ* and RAL measurements are smaller in the upper layer (6-12 km) as compared to the lower layer (0-6 km).

Table 4. The mean and stdv of the difference between *in situ* and IASI RAL partial columns.

in situ	IAGOS		AirCore		HIPPO	
RAL	0-6 km	6-12 km	0-6 km	6-12 km	0-6 km	6-12 km
mean (SAT-AIR) [ppb]	-9.5	-4.9	-22.5	-10.6	-12.2	-1.6
stdv (SAT-AIR) [ppb]	36.0	23.2	27.1	26.1	26.5	22.2
R	0.58	0.51	0.75	0.51	0.87	0.76
N	260	260	49	49	466	466

Atmospheric
Measurement
Techniques
Discussions

The ground-based FTIR (TCCON and NDACC) measurements are used to compare with two IASI CH$_4$ products of RAL and LMD (Table 5). The TCCON and NDACC measurements show that the systematic uncertainties of RAL and LMD data are both within ±10 ppb. However, the stdv of the differences between LMD and FTIR is about 25 ppb, which is larger than that between RAL and FTIR of about 11-16 ppb. The measurements also confirm the strong high latitude biases observed in the comparisons with the CAMS model and the strong seasonal nature of certain biases in the LMD-CAMS comparisons. These seasonal features will be discussed in more detail in the next section. Here we need to add that there are very little stations within the 30°N-30°S latitude band for which the LMD algorithm was initially targeted. Also note that TCCON uses a profile scaling retrieval approach in which the shape of the initial *a priori* profile cannot be altered resulting in potential smoothing errors.

Table 5. The mean station bias and mean station stdv of the difference between ground-based FTIR and IASI satellite CH$_4$ measurements (SAT-GB).

Satellite	LMD		RAL	
	mean	std	mean	std
TCCON	-4.76 ppb	24.00 ppb	4.31 ppb	11.28 ppb
NDACC	1.83 ppb	26.46 ppb	9.55 ppb	15.82 ppb

5   Long-term trend and seasonal variation

Prior to the discussion of the results below, it should be noted that during the course of the analysis, it was found that a discontinuity in RAL L2 data existed due to the change in L1 input data in mid-2013. This change is discussed in Section 5.4 and reported in the RAL product user guide (https://catalogue.ceda.ac.uk/uuid/f717a8ea622f495397f4e76f777349d1; last access: 12 January 2023). However to explore the impact of this discontinuity we performed the intercomparisons without (Section 5.1 and 5.2) and with (Section 5.4) corrections.

5.1   LMD vs RAL

The CH$_4$ annual growths derived from LMD and uncorrected RAL (thus ignoring the discontinuity) are compared to each other (Figure 10). Due to the cloud contamination and post-filtering, the CH$_4$ measurements are not always available even though we use the monthly averaged data. In this section, we only consider the trend on the 1x1° grid where there are less than 12 absent monthly means during these 8 years. The mtCH$_4$ trends derived from the LMD data are generally available in the low-latitude regions, while the XCH$_4$ trends derived from the RAL are calculated in most places except for the polar region. The mean and stdv of the CH$_4$ annual growth rates are 6.43±1.34 ppb/yr and 4.06±0.66 ppb/yr derived from the LMD and RAL data, respectively. The mean difference in CH$_4$ trend from LMD and RAL measurements is 2.54 ppb/yr, which is larger than the stdv of their differences of 1.53 ppb/yr. After smoothing the RAL data with LMD weighting function (RAL_LMDavk), the mtCH$_4$ trend derived from the RAL_LMDavk is 4.29±0.86 ppb/yr, which is larger than the XCH$_4$ trend derived from the original

RAL data. The mean difference in mtCH$_4$ trend between LMD and RAL_LMDavk reduces to 1.63 ppb/yr, which is still larger than the stdv of their differences (1.33 ppb/yr).

The global maps of CH$_4$ annual growth rates are also derived from LMD and RAL night-time measurements (not shown here). The spatial distributions of CH$_4$ trend derived from the daytime and night-time measurements are similar for both LMD
5 and RAL. Moreover, the global mean and stdv of the CH$_4$ trend derived from night-time measurements are 6.65 and 1.46 ppb/yr derived from the LMD data, and are 4.01 and 0.68 ppb/yr derived from the RAL data, which are close to the results derived from daytime measurements. As the results from daytime and night-time measurements are consistent, we only discuss the trends of CH$_4$ derived from the RAL and LMD daytime measurements in the following sections.

The time series and seasonal variation of CH$_4$ are investigated based on the TransCom (Figure 11), which has been used in the
10 Carbon Tracker-CH$_4$ model, including 11 land (Figure 12) and 11 ocean (Figure 13) regions. Here, we mainly focus on LMD and RAL_LMDavk mtCH$_4$ measurements. It is found that the seasonal variations of mtCH$_4$ from LMD and RAL_LMDavk measurements are generally close to each other in the low-latitude regions, but are different in the high-latitude regions. Specifically, the seasonal variations of mtCH$_4$ from LMD and RAL_LMDavk measurements are close to each other in South American Tropical, South American Temperate, Northern Africa, Eurasia Temperate and Tropical Asia, while they are different
15 at North American Boreal, North American Temperate, Europe, Southern Africa, Eurasia Boreal and Australia. The mtCH$_4$ annual growths derived from LMD are 0.4-1.8 ppb/yr larger than RAL_LMDavk in most regions except at North American Boreal and Eurasia Boreal. The mtCH$_4$ annual growth derived from LMD has a strong latitude dependence, which is close to 6 ppb/yr in the tropical region but less than 3 ppb/yr in the high-latitude regions. At ocean regions, it is found that the seasonal variations of mtCH$_4$ from LMD and RAL_LMDavk measurements are close to each other in most regions, except for the
20 Northern Ocean and North Atlantic Temperate. At the Southern Ocean and South Pacific Temperate, the phases of the seasonal variations of mtCH$_4$ from LMD and RAL_LMDavk measurements are similar, but the amplitudes of the seasonal variation of mtCH$_4$ derived from LMD measurements are larger than those derived from the RAL_LMDavk data. The mtCH$_4$ annual growths derived from LMD are 0.3-2.2 ppb/yr larger than RAL_LMDavk in most ocean regions except at the Southern Ocean.

5.2 RAL vs ground-based FTIR measurements

25 The seasonal variations and long-term trends of XCH$_4$ observed by co-located anomaly-uncorrected RAL and TCCON measurements are shown in Figure 14. The XCH$_4$ trends derived from RAL are systematically lower than those derived from TCCON measurements at almost all sites. The mean XCH$_4$ annual growth rates are 4.1 ppb/yr derived from the RAL measurements, and 6.4 ppb/yr derived from TCCON measurements. Note that, due to the limited co-located RAL and TCCON measurements at Eureka, Rikubetsu and Edwards (Figure 8), the uncertainties of the trends at these sites are relatively large.
30 In general, both the phase and amplitudes of the seasonal variations of XCH$_4$ observed by RAL and TCCON are close to each other.

The seasonal variations and long-term trends of XCH$_4$ observed by RAL and NDACC measurements are shown in Figure 15. It is found that the XCH$_4$ trends derived from RAL are close to those derived from NDACC measurements at Eureka, Thule, Jungfraujoch, Zugspitze and Manua Loa, but lower than those derived from NDACC measurements at Kiruna, St Petersburg,

Atmospheric
Measurement
Techniques
Discussions
Open Access

EGU

Garmisch, Izana, Stdenis, Wollongong and Lauder. The mean of the XCH_4 trends derived from the RAL data is 3.8 ppb/yr, which is less than that from NDACC measurements of 5.1 ppb/yr. The phases and amplitudes of the seasonal variations of XCH_4 observed by RAL and NDACC are similar at most sites, which is consistent with the TCCON measurements.

5.3 LMD vs ground-based FTIR measurements

5 The seasonal variations and long-term trends of $mtCH_4$ observed by LMD and TCCON measurements are shown in Figure 16. The $mtCH_4$ trends derived from LMD and TCCON measurements are close to each other at Sodankyla, Bremen, Orleans, Pasadena, Saga, Izana, Ascension, Darwin, Reunion and Wollongong. However, the $mtCH_4$ trends derived from LMD measurements are less than those derived from TCCON measurements at Bialystok, Karlsruhe, Garmisch, Park Falls, Lamont, Tsukuba, and Lauder. In summary, the TCCON measurements indicate that the $mtCH_4$ derived from LMD is underestimated
10 in the higher-latitude regions.

If we only consider LMD's core latitude region (30°N-30°S) (Izana, Ascension, Darwin and Reunion), the mean and stdv of the $mtCH_4$ trends are 6.4±0.9 ppb/yr derived from TCCON measurements, and 6.0±1.8 ppb/yr derived from LMD measurements. Concerning the seasonal variation of the $mtCH_4$, the differences between the LMD and TCCON measurements are obvious at Bialystok, Karlsruhe, Garmisch (European sites), Park Falls, Lamont (American sites), Reunion and Lauder. For
15 example, at Park Falls, the $mtCH_4$ observed by LMD is high in July and low in January, but the $mtCH_4$ observed by TCCON measurement is low in July and high in January. Moreover, the amplitude of the seasonal variation at Park Falls observed by LMD is about 80 ppb, which is 4 times larger than that observed by TCCON measurements of about 20 ppb. These differing seasonal patterns lead to the biases as observed in Figure 9 (LMD-TCCON and NDACC) and Figure 4 (top row, LMD-CAMS), with significant negative biases in autumn-winter and positive biases in summer over the United States and (less outspoken)
20 Europe.

The seasonal variations and long-term trends of $mtCH_4$ observed by LMD and NDACC measurements are shown in Figure 17. The $mtCH_4$ trends derived from LMD are generally less than those from NDACC measurements at mid and high-latitude sites, e.g., Garmisch, Zugspitze, Jungfraujoch, Lauder, Thule, and Eureka. In tropical region, the $mtCH_4$ trends derived from LMD are larger than that from the NDACC measurements at Mauna Loa and Reunion, but are smaller than that from NDACC
25 measurements at Izana. The seasonal variations of $mtCH_4$ observed by LMD and NDACC are similar at Kiruna, Izana, Mauna Loa and Wollongong. However, the seasonal variations of $mtCH_4$ observed by LMD and NDACC are different at Garmisch, Zugspitze, Jungfraujoch (European sites), and Reunion. Both TCCON and NDACC measurements suggest that there is large uncertainty in the seasonal variation of $mtCH_4$ observed by LMD in Europe and Reunion.

5.4 The discontinuity in RAL data after 16 May 2013

30 The above analysis shows that the annual growth of XCH_4 derived from the uncorrected RAL data between July 2007 and June 2015, while generally consistent between regions, is significantly underestimated. Figure 18 clearly shows that, due to a change in the processing of the spectral response model on 16 May 2013, a 7 ppb discontinuity occurred in RAL's retrieved total column methane. Note that no such effect is visible in the LMD data. While a simple overall bias correction was explored

as an option, it was quickly found that the impact of the anomaly had a small latitudinal as well as a significantly differing impact on its partial column values. Therefore, unfortunately, RAL's trend estimates need to be based on 2 individual linear trends for the two periods before and after 16 May 2013. You can then average, using the covered time frames as weights, the two estimates to get the whole period between July 2007 and June 2015 estimates from RAL data before and after 16 May 2013.

Table 6 lists all the trends of CH_4 between July 2007 and June 2015 derived from LMD, RAL_LMDavk and RAL_LMDavk (corrected) at 9 TransCom low-and mid-latitude land regions. The weighted mean of the annual growths of XCH_4 becomes 5.6 ppb/yr by using the RAL data before and after 16 May 2013. Both results are close to the $mtCH_4$ annual growth of 5.3 ppb/yr between July 2007 and June 2015 observed by the LMD data. Thanks to the high data density of RAL, it is robust to derive the XCH_4 annual growth even with 2-years' satellite data (June 2013 - June 2015). The mean XCH_4 annual growth derived from the RAL data between July 2013 and June 2015 is 9.5 ppb/yr, which is larger than that of 4.4 ppb/yr between July 2007 and May 2013. The CH_4 annual growth rate derived from the NOAA surface *in situ* measurements between June 2013 and June 2015 is 11.2 ppb/yr, which is also larger than that of 5.6 ppb/yr between July 2007 and May 2013. The XCH_4 trends estimated from RAL measurements are generally consistent with the NOAA *in situ* measurements.

Table 6. The trend of CH_4 in unit of ppb/yr between July 2007 and June 2015 derived from LMD, RAL_LMDavk and RAL_LMDavk (corrected) at 9 TransCom low- and mid-latitude land regions.

Region	LMD	RAL_LMDavk	RAL_LMDavk (corrected)	
			2007.7-2013.5	2013.6-2015.6
North American Temperate	4.8±0.8	4.2±0.7	4.1±1.5	9.3±4.1
South American Tropical	5.0±1.1	3.8±0.7	4.2±1.2	10.0±6.6
South American Temperate	5.2±0.7	4.4±0.5	4.0±0.5	12.4±5.5
Europe	4.0±1.0	3.6±0.7	3.8±1.4	6.2±2.1
Northern Africa	5.5±1.2	4.5±0.7	4.5±1.5	9.1±1.8
Southern Africa	6.3±0.8	4.5±0.9	4.5±1.1	11.8±7.8
Eurasia Temperate	4.9±1.4	4.1±0.9	4.3±1.6	7.5±4.8
Tropical Asia	5.7±1.3	4.4±0.8	5.3±1.3	9.6±5.5
Australia	6.0±0.6	4.5±0.5	4.5±0.9	9.4±1.9
mean	5.3	4.2	4.4	9.5
			5.6	

6 Discussions

6.1 Two partial columns derived from RAL

In Section 4.1, it is found that the RAL XCH_4 is about 16.5 ppb underestimated between 15°N and 15°S as compared to HIPPO measurements, and the underestimation is mainly coming from the lower partial column (0-6 km). The DOFS of RAL indicate that, apart from the higher latitudes (>60° North and South), 2 independent partial columns can be obtained from the retrieved profiles. Unfortunately, the reference dataset remains fairly limited with regards to accurately assessing partial column information. Not enough vertical profile information is available in the ground-based FTIR measurements. As for the *in situ* observations, they have limited temporal-spatial coverage. Therefore, in this section, we calculate for both RAL and the smoothed CAMS profiles the partial columns between 0-6 km (lower layer) and 6-12 km (upper layer), and we have taken 2012 as an example year to compare RAL with the CAMS model. Here we also need to point out that the RAL product comes with a 50 layer column averaging kernel, but the profile averaging kernel is a 5x50 matrix where the smallest dimension corresponds with the lowest 5 levels of a coarser 12 level retrieval pressure grid. The 3 lowest levels of this lower resolution grid correspond with 1000 hPa, 422 hPa and 178 hPa respectively. The latter 2 pressure levels correspond with the limits of the 0-6 and 6-12 km altitude range of the partial columns. While these pressure ranges roughly contain 1 DOF each, one cannot specifically select, due to the low-resolution grid, the partial column vertical range based on the DOF for each measurement and therefore we cannot state that these column layers are fully independent in all cases.

Figure 19 shows the differences between RAL and CAMS qCH_4 values in the upper and lower layers in January, April, July and October 2012. The mean and stdv of the differences are only calculated for the low- and mid-latitude regions (<60° North and South). It is apparent that the qCH_4 observed by RAL is generally 3.1-8.0 ppb larger than the CAMS model in the upper layer and 5.5-7.7 ppb lower than the CAMS model in the lower layer. Specifically, the RAL qCH_4 in the lower layer is generally lower than the CAMS model in the Mediterranean area, tropics, east Asia and south America, depending on the month of year. The mean underestimation in the Pacific Ocean between 15°N and 15°S during these 4 months is 12.5 ppb less than the CAMS model, which is consistent with the comparison between the HIPPO and RAL in the lower layer. Based on the stdv of the differences, the spatial variability between the RAL and CAMS qCH_4 in the upper layer is less than that in the lower layer. The difference of qCH_4 between the upper and lower layers from RAL and CAMS are also shown in Figure 19. For RAL the mean upper-lower difference ranges between 6.3 and 16.5 ppb, while for CAMS the bias ranges between -5.7 and 7.3 ppb. For CAMS, in most conditions, the difference between upper and lower qCH_4 is either very small or the lower layer yields higher concentrations than the upper layer. A notable exception is the band of positive bias values located around the Southern hemisphere sub-tropics, which is more pronounced in summer than in winter. This latitudinal structure is equally captured by RAL, but the difference between upper and lower qCH_4 is far more pronounced in a far wider region throughout the whole year, also peaking in summer and autumn. Note that none of these features are inherent to the RAL *a priori*, which exhibits a uniform near 0 partial column bias apart from the polar regions where the lower partial column is 25 ppb higher than the upper partial column, and this probably stems from the lack of sufficient spectral information.

Also apparent is the often stark contrast between adjacent land and sea measurements. Some striking examples of this situation are Australia in October and Northern Europe in April. These features are not replicated in the CAMS partial column biases, which shows (as expected) a smooth transition from land to sea, even though the relevant averaging kernel smoothing has been applied. While we expect differences in sensitivity to occur between land and sea measurements (a change in the retrieval uncertainty and with that the DOF is expected), ideally the impact thereof is translated into the averaging kernel. Note that these features are not clearly present in the LMD and RAL total column product.

Apart from the uncertainties within the CAMS model, there might be many reasons for the observed partial column differences from the RAL retrieval such as the uncertainty of the spectroscopy, meteorological parameters etc., which could potentially affect partial columns differently. In addition, optimal estimation retrievals rely on a fine balance between placing too much constraint on the retrieval, resulting in too little retrieval information being added to the *a priori* and thus lower degrees of freedom on the one hand and placing not enough constraints on the retrieval, which risks producing unrealistic retrieval results. The latter often presents itself most clearly in unrealistic vertical retrieval profiles. Other observations that indicate a large sensitivity on the measured radiances are the 7 to 8 ppb bias between IFOV 1 and IFOV 3 of IASI, the 7 ppb to 12 ppb (for the total and lower partial column specifically) bias shift due to the change in L1 data on the 16th of May 2013, and the above mentioned stark contrast between the upper and lower partial column bias between adjacent land and sea measurements. If true, additional constraints need to be added to the retrieval, thereby adding stability at the cost of degrees of freedom, potentially losing the capacity to resolve two independent layers. Another factor that might be at play is the limited vertical resolution of the retrieved profile and associated averaging kernel. Both partial columns effectively correspond with 1.5 layers in the profile, which leaves little room for accurately capturing any potential variability in the sensitivity within each layer, nor does it ensure true independence between the partial columns. Further investigation is needed to understand the performance of the RAL two partial columns better, when more *in situ* data become available.

6.2 LMD seasonal cycle discussion

By comparing LMD with RAL, CAMS, HIPPO and ground-based FTIR measurements, it is found that the seasonal variation of mtCH$_4$ observed by LMD is different from others, especially in certain latitude regions (see Figure 4). However CAMS model data can hardly be regarded as the true state of the atmosphere, only an approximation thereof. And while HIPPO measurements are highly accurate, they need to be expanded by model profiles to cover LMD's entire vertical sensitivity range. Changing the CAMS UTLS transition region resulted in significant changes in the observed biases with HIPPO. We can only point to the fact that the changes we needed to make to the CAMS profile in order to overcome the observed biases were not insignificant (but not impossible either). Ground-based remote sensing TCCON FTIR measurements does not need model profile extensions but it uses a profile scaling retrieval approach and since the shape of the profile is of great influence when applying LMD's sensitivity profile, one could certainly cast doubt on these observed biases as well. One can only point out that they confirm the HIPPO and CAMS observations even though they use a different approach to construct their *a priori* profile shape. NDACC FTIR retrievals on the other hand use an optimal estimation approach which allows for profile shape optimization and here again we observe seasonal bias variability at, for instance, the Jungfraujoch data. Unfortunately its vertical profile resolution

is very limited (DOF's is about 2.5) and one could claim that this is insufficient for an accurate application of the LMD sensitivity profile. Therefore in this section, we use the AirCore profiles at Boulder (39.7°N, 104.8°W) as the reference data to compare with the CAMS model and the LMD measurements. The AirCore profiles at Boulder are selected because the seasonal variations of CH_4 observed by LMD and RAL are very different at North American Template region (Figure 13). There are 5

5   AirCore measurements available at Boulder between October 2017 and September 2019. Figure 20 shows the AirCore vertical profiles, and the $mtCH_4$ derived from these AirCore profiles with the smoothing correcting using the LMD weighting function. The AirCore profile has a good vertical coverage, providing measurements between the surface and the stratosphere (about 25 km) so no (potentially flawed) model data is required to extend its profile over the troposphere-stratosphere boundary where a sharp decrease in CH_4 occurs. The seasonal variation of $mtCH_4$ derived from the LMD measurements within ±5° latitude

10   and ±5° longitude around Boulder between June 2007 and June 2015 show that $mtCH_4$ is high in summer and low in winter. However, the AirCore measurements show that the $mtCH_4$ is low in summer and high in autumn and winter, which is consistent with the TCCON measurements at Lamont (Figure 16). The CAMS model at Boulder shows a seasonal cycle phase that is in line with the AirCore measurements although its amplitude looks underestimated. Since we see a clear latitudinal dependence of both the long term trend as well as the seasonal cycle offset we have likewise obtained the long term trend and seasonal

15   cycles of the SAT-CAMS biases, grouped per 10° latitude band. The results thereof are shown in Figure 21. It shows that the amplitude of the seasonal cycle in the RAL-CAMS residuals is consistently lower than for LMD. Note that, as shown above, the CAMS seasonal cycle may not be accurate itself. However what is more of interest is that we see a strong increase in the LMD residual seasonal amplitudes at higher (>50°) latitudes. Likewise for the long term trend, RAL (both versions) shows little variability in the long term trend of the RAL-CAMS residuals, whereas LMD shows a very strong decrease in the residual

20   trend at latitudes exceeding (40°) in both hemispheres.

To conclude, while we accept that the used dataset is very limited, combined with all the other observations, AirCore measurements strongly suggest that the seasonal variation of $mtCH_4$ observed by LMD retrievals have a significant overestimation of the seasonal amplitude together with a misrepresentation of the phase and an underestimation of the long term trend above several higher-latitude regions. This observed decrease in fidelity at higher latitudes calls for an investigation of the robustness

25   of LMD's Neural Network training database for these scenes. This is acknowledged by the algorithm development team as it currently advises users to be cautious when handling data from latitudes beyond 60° North and South. Our analysis however shows that even at lower latitudes timeseries start becoming less robust as compared to the 35°N-35°S latitude band.

7   Conclusions

The goal of this study was to perform an extensive validation of two IASI global CH_4 products (RAL and LMD) between July

30   2007 and June 2015, using a wide array of reference measurements.

The IASI products are compared to *in situ* and ground-based FTIR data. Average differences with respect to *in situ* measurements for LMD range between -0.3 and 10.9 ppb, while for RAL they range between -10.2 and -4.6 ppb. For the *in situ* comparisons, the differences from RAL are consistently more negative than those from LMD. The stdv of the observed dif-

ferences are consistently smaller for RAL. For AirCore, these differences are small. For IAGOS and HIPPO, these differences are more substantial. Moreover, it is found that there is about 16.5 ppb underestimation in XCH_4 for RAL measurement in the tropics, which is mainly coming from the lower layer between 0 and 6 km. Using the ground-based FTIR sites as the reference data, the mean stdv of the differences at the ground-based stations show significantly lower values for RAL (11-16
5 ppb) than those for LMD (about 25 ppb). Looking at the latitudinal and seasonal variability at TCCON and NDACC sites, we observe that RAL tends to overestimate XCH_4 over the high-latitude sites, while LMD data is on average larger than TCCON measurements in the tropical region and smaller than TCCON measurements at mid-latitude sites.

An analysis of the long-term stability and seasonal cycles of the LMD and RAL products was carried out. We observed significant differences between the two algorithms. For RAL, we initially observed a significant underestimation of the long-
10 term trend. This is due to an anomaly occurring on 16 May 2013 (due to a change in the IASI level 1 product) which caused a significant bias shift. The L1 discontinuity in May 2013 is solved by using reprocessed L1 data, which have been acquired and RAL is indeed now using. For LMD we observed significant deviations (with respect to RAL and the reference data), of the seasonal cycle (both in the magnitude of the amplitude as well as its phase) over several higher (>35°)-latitude regions. We also found an underestimation of the long-term trend at higher latitudes. All in all this results in large seasonal biases at these
15 sites during the later years of the timeseries.

Users should also be aware that, while the RAL partial columns manage to capture global features, they also still exhibit significant systematic errors. This observation, combined with the sensitivity of the retrieval with respect to the IASI L1 data and detector pixel, also poses the question whether the RAL Optimal Estimation retrieval requires more constraint. On the other hand, imposing a stronger prior constraint would result in more accurate retrieved values only if the "true" CH_4 distribution
20 was adopted as the prior. Improvements to the scheme used to produce the data which have been evaluated here have also been made, and the negative bias at low latitudes thereby reduced. Further improvements to address the positive bias at high latitudes and other issues will be implemented for the next full reprocessing.

Author contributions. BD acted as the project PI. The validation work was carried out by BD, MZ, PP and YK with support from BL,
30 CCP, CS and MDM. BK and RS provided RAL data and interacted with the validation team. MZ and BD prepared the paper. All authors contributed to the discussion and revision of the paper.

Competing interests. The authors declare that they have no conflict of interest.

References

Agusti-Panareda, A., Diamantakis, M., Bayona, V., Klappenbach, F., and Butz, A.: Improving the inter-hemispheric gradient of total column atmospheric CO_2 and CH_4 in simulations with the ECMWF semi-Lagrangian atmospheric global model, Geoscientific Model Development, 10, 1–18, https://doi.org/10.5194/gmd-10-1-2017, 2017.

5 Andersen, T., Scheeren, B., Peters, W., and Chen, H.: A UAV-based active AirCore system for measurements of greenhouse gases, Atmospheric Measurement Techniques, 11, 2683–2699, https://doi.org/10.5194/amt-11-2683-2018, 2018.

Baier, B., Sweeney, C., Tans, P., Newberger, T., Higgs, J., and Wolter, S.: NOAA AirCore atmospheric sampling system profiles (Version 20210813) [Data set], https://doi.org/https://doi.org/10.15138/6AV0-MY81, 2021.

Blumenstock, T., Hase, F., Schneider, M., García, O. E., and Sepúlveda, E.: TCCON data from Izana (ES), Release GGG2014.R1,
10   https://doi.org/10.14291/TCCON.GGG2014.IZANA01.R1, https://data.caltech.edu/records/302, 2017.

Crevoisier, C., Nobileau, D., Fiore, A. M., Armante, R., Chédin, A., and Scott, N. A.: Tropospheric methane in the tropics – first year from IASI hyperspectral infrared observations, Atmos. Chem. Phys., 9, 6337–6350, https://doi.org/10.5194/acp-9-6337-2009, 2009.

Crevoisier, C., Nobileau, D., Armante, R., Crépeau, L., Machida, T., Sawa, Y., Matsueda, H., Schuck, T., Thonat, T., Pernin, J., Scott, N. A., and Chédin, A.: The 2007–2011 evolution of tropical methane in the mid-troposphere as seen from space by MetOp-A/IASI, Atmos.
15   Chem. Phys., 13, 4279–4289, https://doi.org/10.5194/acp-13-4279-2013, 2013.

De Mazière, M., Sha, M. K., Desmet, F., Hermans, C., Scolas, F., Kumps, N., Metzger, J.-M., Duflot, V., and Cammas, J.-P.: TCCON data from Réunion Island (RE), Release GGG2014.R1, https://doi.org/10.14291/TCCON.GGG2014.REUNION01.R1, https://data.caltech. edu/records/322, 2017.

De Mazière, M., Thompson, A. M., Kurylo, M. J., Wild, J. D., Bernhard, G., Blumenstock, T., Braathen, G. O., Hannigan, J. W., Lambert,
20   J.-C., Leblanc, T., McGee, T. J., Nedoluha, G., Petropavlovskikh, I., Seckmeyer, G., Simon, P. C., Steinbrecht, W., and Strahan, S. E.: The Network for the Detection of Atmospheric Composition Change (NDACC): history, status and perspectives, Atmos. Chem. Phys., 18, 4935–4964, https://doi.org/10.5194/acp-18-4935-2018, 2018.

Deutscher, N. M., Notholt, J., Messerschmidt, J., Weinzierl, C., Warneke, T., Petri, C., and Grupe, P.: TCCON data from Bialystok (PL), Release GGG2014.R2, https://doi.org/10.14291/TCCON.GGG2014.BIALYSTOK01.R2, https://data.caltech.edu/records/1300, 2019.

25 Dlugokencky, E. J., Steele, L. P., Lang, P. M., and Masarie, K. A.: The growth rate and distribution of atmospheric methane, J Geophys Res Atmos., 99, 17 021–17 043, https://doi.org/https://doi.org/10.1029/94JD01245, 1994.

Edwards, P. G., Berutti, B., Blythe, P., Callies, J., Carlier, S., Fransen, C., Krutsch, R., Lefebvre, A.-R., Loiselet, M., and Stricker, N.: The MetOp satellite - Weather information from polar orbit, ESA Bulletin, 127, 8–17, 2006.

Feist, D. G., Arnold, S. G., John, N., and Geibel, M. C.: TCCON data from Ascension Island (SH), Release GGG2014.R0,
30   https://doi.org/10.14291/TCCON.GGG2014.ASCENSION01.R0/1149285, https://data.caltech.edu/records/210, 2014.

Filges, A., Gerbig, C., Chen, H., Franke, H., Klaus, C., and Jordan, A.: The IAGOS-core greenhouse gas package: a measurement system for continuous airborne observations of CO2, CH4, H2O and CO, Tellus B Chem. Phys. Meteorol., 67, 27 989, https://doi.org/10.3402/tellusb.v67.27989, 2015.

Griffith, D. W., Deutscher, N. M., Velazco, V. A., Wennberg, P. O., Yavin, Y., Keppel-Aleks, G., Washenfelder, R. A.,
35   Toon, G. C., Blavier, J.-F., Paton-Walsh, C., Jones, N. B., Kettlewell, G. C., Connor, B. J., Macatangay, R. C., Roehl, C., Ryczek, M., Glowacki, J., Culgan, T., and Bryant, G. W.: TCCON data from Darwin (AU), Release GGG2014.R0, https://doi.org/10.14291/TCCON.GGG2014.DARWIN01.R0/1149290, https://data.caltech.edu/records/269, 2014a.

Atmospheric
Measurement
Techniques
Open Access

EGU

Discussions

Griffith, D. W., Velazco, V. A., Deutscher, N. M., Paton-Walsh, C., Jones, N. B., Wilson, S. R., Macatangay, R. C., Kettlewell, G. C., Buchholz, R. R., and Riggenbach, M. O.: TCCON data from Wollongong (AU), Release GGG2014.R0, https://doi.org/10.14291/TCCON.GGG2014.WOLLONGONG01.R0/1149291, https://data.caltech.edu/records/291, 2014b.

Hase, F., Hannigan, J., Coffey, M., Goldman, A., Höpfner, M., Jones, N., Rinsland, C., and Wood, S.: Intercomparison of retrieval
5 codes used for the analysis of high-resolution, ground-based FTIR measurements, J. Quant. Spectrosc. Radiat. Transf., 87, 25 – 52, https://doi.org/10.1016/j.jqsrt.2003.12.008, 2004.

Hase, F., Blumenstock, T., Dohe, S., Groß, J., and Kiel, M.: TCCON data from Karlsruhe (DE), Release GGG2014.R1, https://doi.org/10.14291/TCCON.GGG2014.KARLSRUHE01.R1/1182416, https://data.caltech.edu/records/278, 2015.

Inness, A., Ades, M., Agustí-Panareda, A., Barré, J., Benedictow, A., Blechschmidt, A.-M., Dominguez, J. J., Engelen, R., Eskes, H., Flem-
10 ming, J., Huijnen, V., Jones, L., Kipling, Z., Massart, S., Parrington, M., Peuch, V.-H., Razinger, M., Remy, S., Schulz, M., and Suttie, M.: The CAMS reanalysis of atmospheric composition, Atmos. Chem. Phys., 19, 3515–3556, https://doi.org/10.5194/acp-19-3515-2019, 2019.

IPCC: Climate change 2013: The physical science basis. Contribution of Working Group I to the Fifth Assessment Report of the Intergovernmental Panel on Climate Change, 2013.

15 Iraci, L. T., Podolske, J. R., Hillyard, P. W., Roehl, C., Wennberg, P. O., Blavier, J.-F., Landeros, J., Allen, N., Wunch, D., Zavaleta, J., Quigley, E., Osterman, G. B., Albertson, R., Dunwoody, K., and Boyden, H.: TCCON data from Edwards (US), Release GGG2014.R1, https://doi.org/10.14291/TCCON.GGG2014.EDWARDS01.R1/1255068, https://data.caltech.edu/records/270, 2016.

Karion, A., Sweeney, C., Tans, P., and Newberger, T.: AirCore: An innovative atmospheric sampling system, J. Atmos. Ocean. Technol., 27, 1839–1853, https://doi.org/10.1175/2010JTECHA1448.1, 2010.

20 Kawakami, S., Ohyama, H., Arai, K., Okumura, H., Taura, C., Fukamachi, T., and Sakashita, M.: TCCON data from Saga (JP), Release GGG2014.R0, https://doi.org/10.14291/TCCON.GGG2014.SAGA01.R0/1149283, https://data.caltech.edu/records/288, 2014.

Kirschke, S., Bousquet, P., Ciais, P., Saunois, M., Canadell, J. G., Dlugokencky, E. J., Bergamaschi, P., Bergmann, D., Blake, D. R., Bruhwiler, L., Cameron-Smith, P., Castaldi, S., Chevallier, F., Feng, L., Fraser, A., Heimann, M., Hodson, E. L., Houweling, S., Josse, B., Fraser, P. J., Krummel, P. B., Lamarque, J.-F., Langenfelds, R. L., Le Quéré, C., Naik, V., O'Doherty, S., Palmer, P. I., Pison, I., Plummer, D., Poulter,
25 B., Prinn, R. G., Rigby, M., Ringeval, B., Santini, M., Schmidt, M., Shindell, D. T., Simpson, I. J., Spahni, R., Steele, L. P., Strode, S. A., Sudo, K., Szopa, S., van der Werf, G. R., Voulgarakis, A., van Weele, M., Weiss, R. F., Williams, J. E., and Zeng, G.: Three decades of global methane sources and sinks, Nat. Geosci., https://doi.org/10.1038/ngeo1955, 2013.

Kivi, R., Heikkinen, P., and Kyrö, E.: TCCON data from Sodankylä (FI), Release GGG2014.R0, https://doi.org/10.14291/TCCON.GGG2014.SODANKYLA01.R0/1149280, https://data.caltech.edu/records/289, 2014.

30 Knappett, D.: RAL IASI MetOp-A TIR Methane Dataset v2.0 Product User Guide. Documentation, Centre for Environmental Data Analysis (CEDA), 2019.

Massart, S., Agusti-Panareda, A., Aben, I., Butz, A., Chevallier, F., Crevosier, C., Engelen, R., Frankenberg, C., and Hasekamp, O.: Assimilation of atmospheric methane products into the MACC-II system: From SCIAMACHY to TANSO and IASI, Atmos. Chem. Phys., 14, 6139–6158, https://doi.org/10.5194/acp-14-6139-2014, 2014.

35 Morino, I., Matsuzaki, T., and Horikawa, M.: TCCON data from Tsukuba (JP), 125HR, Release GGG2014.R2, https://doi.org/10.14291/TCCON.GGG2014.TSUKUBA02.R2, https://data.caltech.edu/records/958, 2018a.

Morino, I., Yokozeki, N., Matsuzaki, T., and Horikawa, M.: TCCON data from Rikubetsu (JP), Release GGG2014.R2, https://doi.org/10.14291/TCCON.GGG2014.RIKUBETSU01.R2, https://data.caltech.edu/records/957, 2018b.

Notholt, J., Petri, C., Warneke, T., Deutscher, N. M., Palm, M., Buschmann, M., Weinzierl, C., Macatangay, R. C., and Grupe, P.: TCCON data from Bremen (DE), Release GGG2014.R1, https://doi.org/10.14291/TCCON.GGG2014.BREMEN01.R1, https://data.caltech.edu/records/1290, 2019.

Ostler, A., Sussmann, R., Rettinger, M., Deutscher, N. M., Dohe, S., Hase, F., Jones, N., and Palm, M.: Multistation intercomparison of column-averaged methane from NDACC and TCCON: Impact of dynamical variability, Atmos. Meas. Tech., 7, 4081–4101, https://doi.org/10.5194/amt-7-4081-2014, 2014a.

Ostler, A., Sussmann, R., Rettinger, M., Deutscher, N. M., Dohe, S., Hase, F., Jones, N., Palm, M., and Sinnhuber, B.-M.: Multistation intercomparison of column-averaged methane from NDACC and TCCON: impact of dynamical variability, Atmos. Meas. Tech., 7, 4081–4101, https://doi.org/10.5194/amt-7-4081-2014, 2014b.

Palmer, P. I., O'Doherty, S., Allen, G., Bower, K., Bösch, H., Chipperfield, M. P., Connors, S., Dhomse, S., Feng, L., Finch, D. P., Gallagher, M. W., Gloor, E., Gonzi, S., Harris, N. R. P., Helfter, C., Humpage, N., Kerridge, B., Knappett, D., Jones, R. L., Le Breton, M., Lunt, M. F., Manning, A. J., Matthiesen, S., Muller, J. B. A., Mullinger, N., Nemitz, E., O'Shea, S., Parker, R. J., Percival, C. J., Pitt, J., Riddick, S. N., Rigby, M., Sembhi, H., Siddans, R., Skelton, R. L., Smith, P., Sonderfeld, H., Stanley, K., Stavert, A. R., Wenger, A., White, E., Wilson, C., and Young, D.: A measurement-based verification framework for UK greenhouse gas emissions: an overview of the Greenhouse gAs Uk and Global Emissions (GAUGE) project, Atmos. Chem. Phys., 18, 11 753–11 777, https://doi.org/10.5194/acp-18-11753-2018, 2018.

Ramonet, M., Langerock, B., Warneke, T., and Eskes, H. J.: Validation report of the CAMS greenhouse gas global reanalysis, years 2003-2016, Copernicus Atmosphere Monitoring Service (CAMS) report, CAMS, https://doi.org/10.24380/y034-7672, 2020.

Rigby, M., Prinn, R. G., Fraser, P. J., Simmonds, P. G., Langenfelds, R. L., Huang, J., Cunnold, D. M., Steele, L. P., Krummel, P. B., Weiss, R. F., O'Doherty, S., Salameh, P. K., Wang, H. J., Harth, C. M., Mühle, J., and Porter, L. W.: Renewed growth of atmospheric methane, Geophys. Res. Lett., 35, L22 805, https://doi.org/10.1029/2008GL036037, 2008.

Rigby, M., Montzka, S. A., Prinn, R. G., White, J. W. C., Young, D., O'Doherty, S., Lunt, M. F., Ganesan, A. L., Manning, A. J., Simmonds, P. G., Salameh, P. K., Harth, C. M., Mühle, J., Weiss, R. F., Fraser, P. J., Steele, L. P., Krummel, P. B., McCulloch, A., and Park, S.: Role of atmospheric oxidation in recent methane growth, Proc. Natl. Acad. Sci., 114, 5373–5377, https://doi.org/10.1073/pnas.1616426114, 2017.

Rodgers, C. D.: Inverse Methods for Atmospheric Sounding – Theory and Practice, Series on Atmospheric Oceanic and Planetary Physics, vol. 2, World Scientific Publishing Co. Pte. Ltd, Singapore, https://doi.org/10.1142/9789812813718, 2000.

Rodgers, C. D. and Connor, B. J.: Intercomparison of remote sounding instruments, J. Geophys. Res., 108, 46–48, https://doi.org/10.1029/2002JD002299, 2003.

Schwietzke, S., Sherwood, O. A., Bruhwiler, L. M. P., Miller, J. B., Etiope, G., Dlugokencky, E. J., Michel, S. E., Arling, V. A., Vaughn, B. H., White, J. W. C., and Tans, P. P.: Upward revision of global fossil fuel methane emissions based on isotope database, Nature, 538, 88–91, https://doi.org/10.1038/nature19797, 2016.

Sherlock, V., Connor, B., Robinson, J., Shiona, H., Smale, D., and Pollard, D. F.: TCCON data from Lauder (NZ), 125HR, Release GGG2014.R0, https://doi.org/10.14291/TCCON.GGG2014.LAUDER02.R0/1149298, https://data.caltech.edu/records/281, 2014.

Siddans, R., Knappett, D., Kerridge, B., Waterfall, A., Hurley, J., Latter, B., Boesch, H., and Parker, R.: Global height-resolved methane retrievals from the Infrared Atmospheric Sounding Interferometer (IASI) on MetOp, Atmos. Meas. Tech., 10, 4135–4164, https://doi.org/10.5194/amt-10-4135-2017, 2017.

Strong, K., Roche, S., Franklin, J. E., Mendonca, J., Lutsch, E., Weaver, D., Fogal, P. F., Drummond, J. R., Batchelor, R., and Lindenmaier, R.: TCCON data from Eureka (CA), Release GGG2014.R3, https://doi.org/10.14291/TCCON.GGG2014.EUREKA01.R3, https://data.caltech.edu/records/1171, 2019.

Sussmann, R. and Rettinger, M.: TCCON data from Garmisch (DE), Release GGG2014.R2, https://doi.org/10.14291/TCCON.GGG2014.GARMISCH01.R2, https://data.caltech.edu/records/956, 2018.

Turner, A. J., Frankenberg, C., Wennberg, P. O., and Jacob, D. J.: Ambiguity in the causes for decadal trends in atmospheric methane and hydroxyl, Proc. Natl. Acad. Sci., 114, 5367–5372, https://doi.org/10.1073/PNAS.1616020114, 2017.

Warneke, T., Messerschmidt, J., Notholt, J., Weinzierl, C., Deutscher, N. M., Petri, C., and Grupe, P.: TCCON data from Orléans (FR), Release GGG2014.R1, https://doi.org/10.14291/TCCON.GGG2014.ORLEANS01.R1, https://data.caltech.edu/records/1301, 2019.

Wennberg, P. O., Wunch, D., Roehl, C. M., Blavier, J.-F., Toon, G. C., and Allen, N. T.: TCCON data from Caltech (US), Release GGG2014.R1, https://doi.org/10.14291/TCCON.GGG2014.PASADENA01.R1/1182415, https://data.caltech.edu/records/285, 2015.

Wennberg, P. O., Roehl, C. M., Blavier, J.-F., Wunch, D., and Allen, N. T.: TCCON data from Jet Propulsion Laboratory (US), 2011, Release GGG2014.R1, https://doi.org/10.14291/TCCON.GGG2014.JPL02.R1/1330096, https://data.caltech.edu/records/277, 2016a.

Wennberg, P. O., Wunch, D., Roehl, C. M., Blavier, J.-F., Toon, G. C., and Allen, N. T.: TCCON data from Lamont (US), Release GGG2014.R1, https://doi.org/10.14291/TCCON.GGG2014.LAMONT01.R1/1255070, https://data.caltech.edu/records/279, 2016b.

Wennberg, P. O., Roehl, C. M., Wunch, D., Toon, G. C., Blavier, J.-F., Washenfelder, R., Keppel-Aleks, G., Allen, N. T., and Ayers, J.: TCCON data from Park Falls (US), Release GGG2014.R1, https://doi.org/10.14291/TCCON.GGG2014.PARKFALLS01.R1, https://data.caltech.edu/records/295, 2017.

WMO: WMO Greenhouse Gas Bulletin | World Meteorological Organization, WMO Bull., https://doi.org/ISSN 2078-0796, 2017.

Wofsy, S. C.: HIAPER Pole-to-Pole Observations (HIPPO): fine-grained, global-scale measurements of climatically important atmospheric gases and aerosols, Philosophical Transactions of the Royal Society A: Mathematical, Physical and Engineering Sciences, 369, 2073–2086, https://doi.org/10.1098/rsta.2010.0313, 2011.

Worden, J. R., Bloom, A. A., Pandey, S., Jiang, Z., Worden, H. M., Walker, T. W., Houweling, S., and Röckmann, T.: Reduced biomass burning emissions reconcile conflicting estimates of the post-2006 atmospheric methane budget, Nat. Commun., 8, 2227, https://doi.org/10.1038/s41467-017-02246-0, 2017.

Wunch, D., Toon, G. C., Wennberg, P. O., Wofsy, S. C., Stephens, B. B., Fischer, M. L., Uchino, O., Abshire, J. B., Bernath, P., Biraud, S. C., Blavier, J. F. L., Boone, C., Bowman, K. P., Browell, E. V., Campos, T., Connor, B. J., Daube, B. C., Deutscher, N. M., Diao, M., Elkins, J. W., Gerbig, C., Gottlieb, E., Griffith, D. W. T., Hurst, D. F., Jiménez, R., Keppel-Aleks, G., Kort, E. A., MacAtangay, R., MacHida, T., Matsueda, H., Moore, F., Morino, I., Park, S., Robinson, J., Roehl, C. M., Sawa, Y., Sherlock, V., Sweeney, C., Tanaka, T., and Zondlo, M. A.: Calibration of the total carbon column observing network using aircraft profile data, Atmos. Meas. Tech., https://doi.org/10.5194/amt-3-1351-2010, 2010.

Wunch, D., Toon, G. C., Blavier, J.-F. L., Washenfelder, R. A., Notholt, J., Connor, B. J., Griffith, D. W. T., Sherlock, V., and Wennberg, P. O.: The Total Carbon Column Observing Network, Philos. Trans. R. Soc. A Math. Phys. Eng. Sci., 369, 2087–2112, https://doi.org/10.1098/rsta.2010.0240, 2011.

Wunch, D., Toon, G. C., Sherlock, V., Deutscher, N. M., Liu, C., Feist, D. G., and Wennberg, P. O.: The Total Carbon Column Observing Network's GGG2014 Data Version, Tech. rep., California Institute of Technology, Pasadena, CA, https://doi.org/10.14291/tccon.ggg2014.documentation.R0/1221662, http://dx.doi.org/10.14291/tccon.ggg2014.documentation.R0/1221662, 2015.

Zhou, M., Langerock, B., Vigouroux, C., Sha, M. K., Ramonet, M., Delmotte, M., Mahieu, E., Bader, W., Hermans, C., Kumps, N., Metzger, J.-M., Duflot, V., Wang, Z., Palm, M., and De Mazière, M.: Atmospheric CO and CH4 time series and seasonal variations on Reunion Island from ground-based in-situ and FTIR (NDACC and TCCON) measurements, Atmos. Chem. Phys., 18, 13 881–13 901, https://doi.org/10.5194/acp-18-13881-2018, 2018.
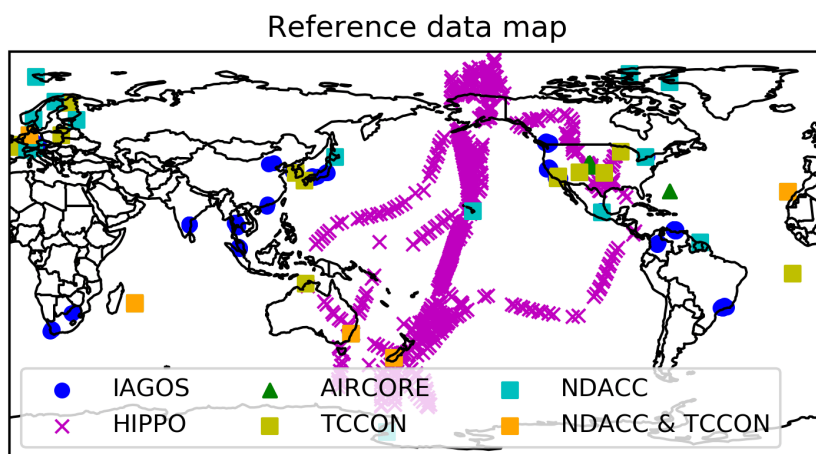
Figure 1. The map of the reference data used in this study, including *in situ* profiles and ground-based FTIR measurements.
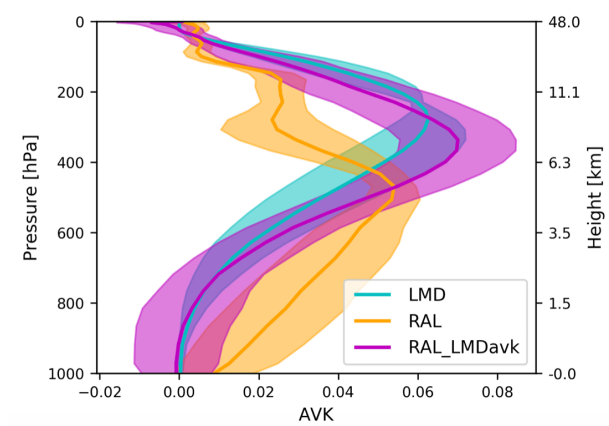
Figure 2. The vertical sensitivities of LMD, RAL and RAL but smoothed with the column averaging kernel of LMD (RAL_LMDavk). The solid data is the global annual mean in 2014, and the shadow is the standard deviation of all the averaging kernels in 2014.
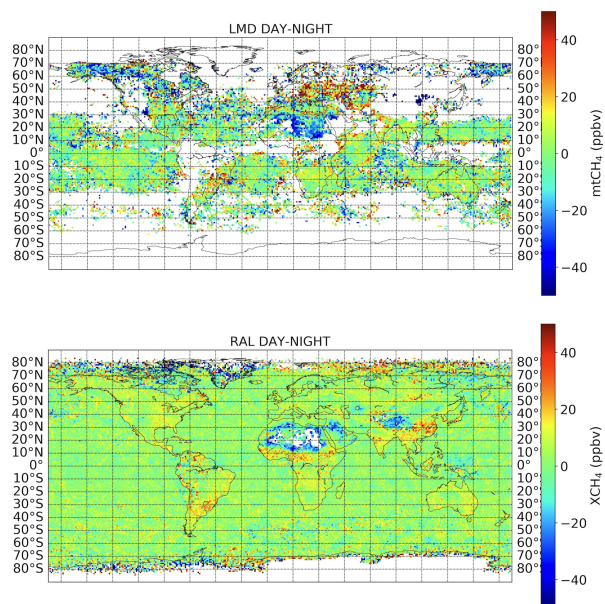
Figure 3. monthly averaged LMD Day-Night mtCH$_4$ (top) and column averaged RAL (bottom) Day-Night XCH$_4$ differences for April 2012
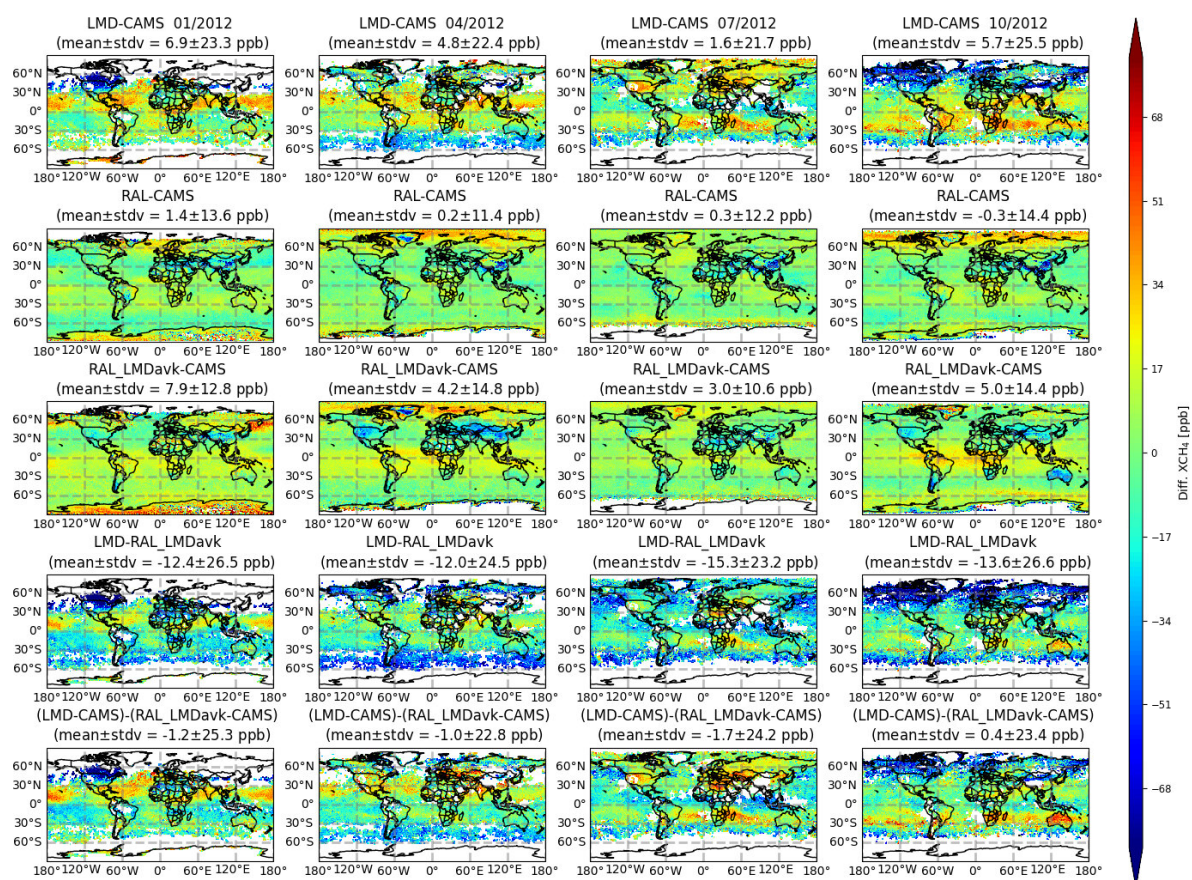
Figure 4. Global monthly mean maps for January, April, July and October 2012 (from left to right column). The top row shows the LMD-CAMS daytime mtCH$_4$ difference, the second and third row show the same but for RAL and RAL_LMDavk X(mt)CH$_4$ respectively. The last three rows show the intercomparison between the satellite products. Row 4 shows the LMD-RAL difference, row 5 LMD-RAL_LMDavk, while the bottom row compares the respective differences of LMD and RAL_LMDavk to their respective CAMS fields.

Atmospheric
Measurement
Techniques
Discussions
Open Access
EGU
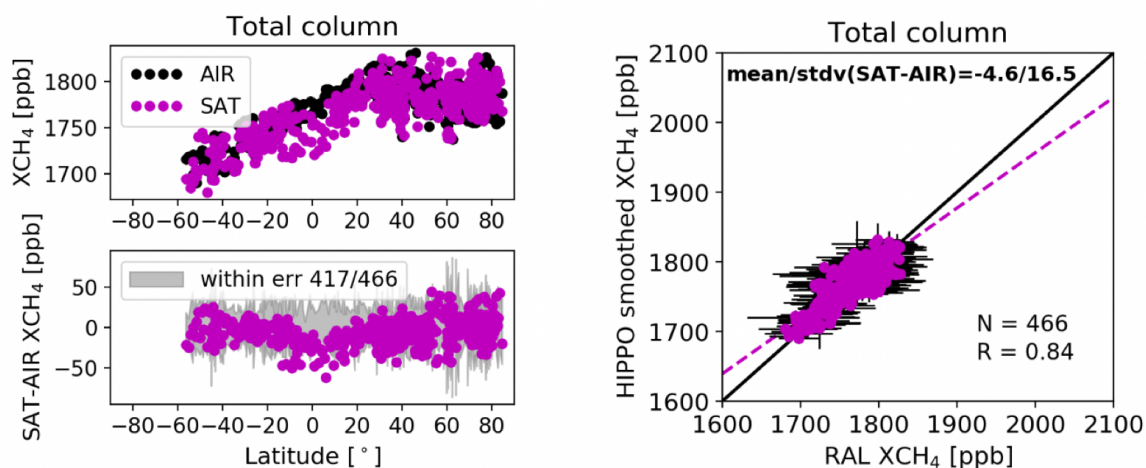
Figure 5. RAL and HIPPO XCH$_4$ together with their differences at different latitudes (left), and the scatter plot between the RAL and HIPPO XCH$_4$. N is the number of co-located data pair and R is the correlation efficient.
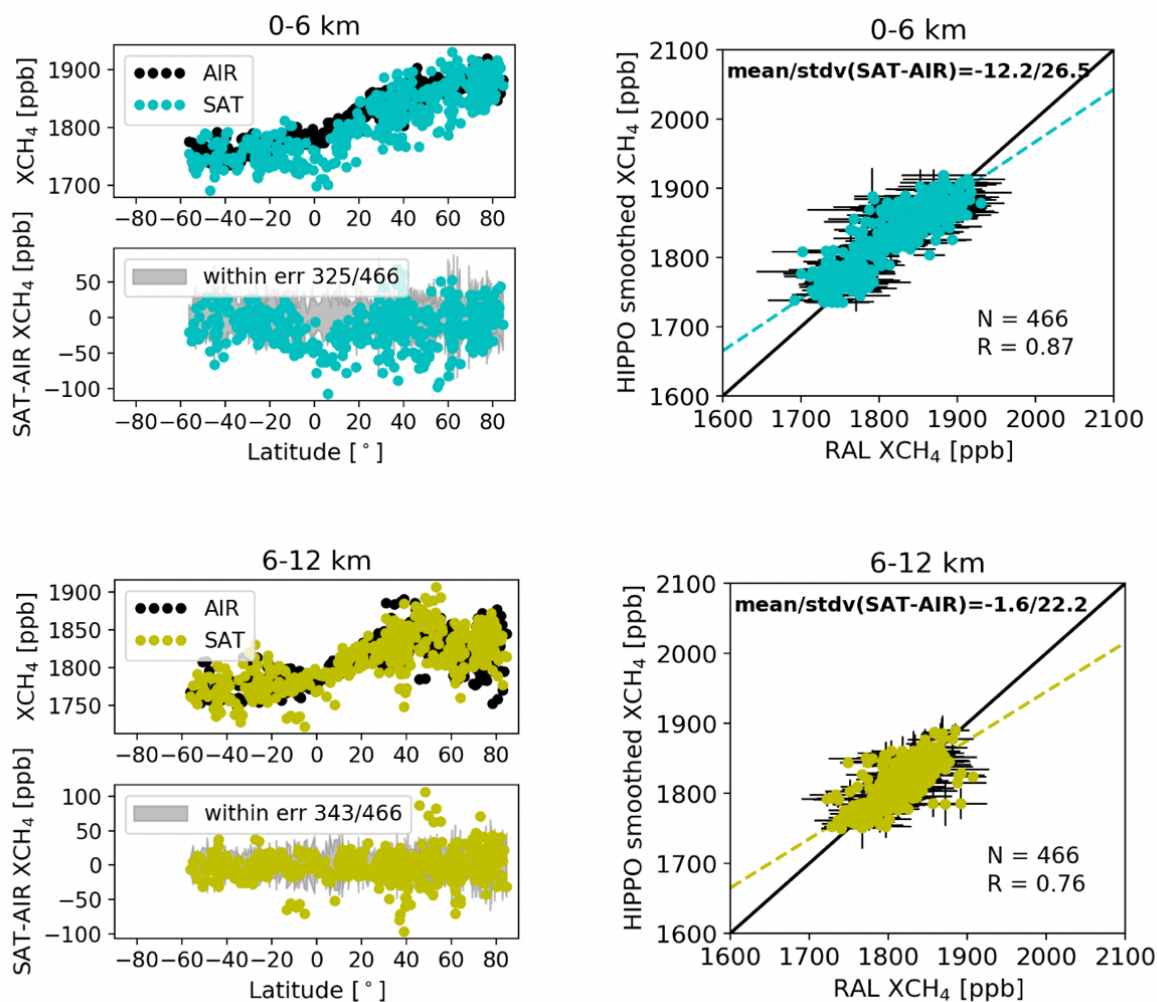
Figure 6. RAL and HIPPO qCH$_4$ together with their differences at different latitude (left), and the scatter plot between the satellite and HIPPO qCH$_4$ in the vertical ranges between 0 and 6 km (upper panels), and between 6 and 12 km (lower panels). N is the number of co-located data pair and R is the correlation efficient.

Atmospheric
Measurement
Techniques
Discussions
Open Access
EGU
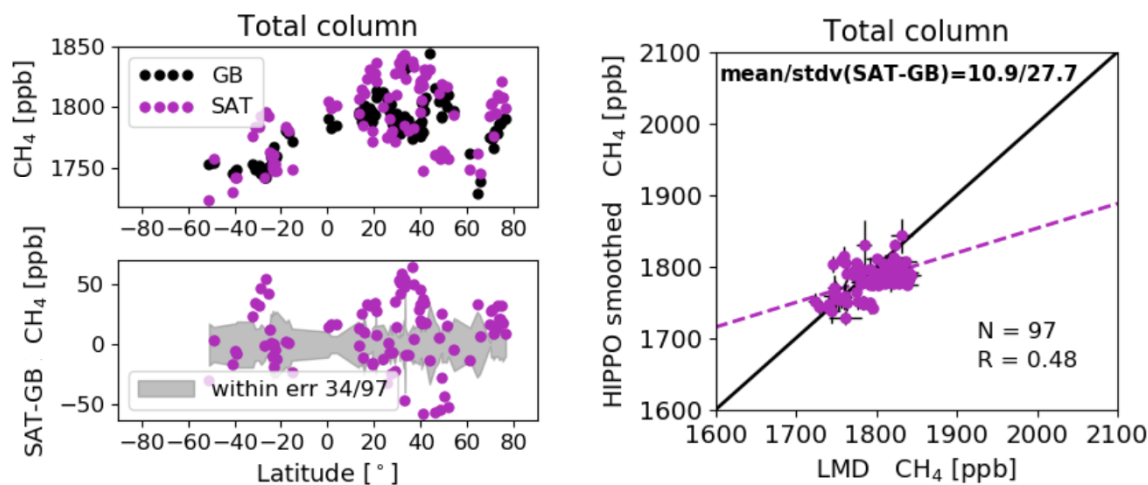
Figure 7. Same as Figure 5, but for HIPPO and LMD measurements.
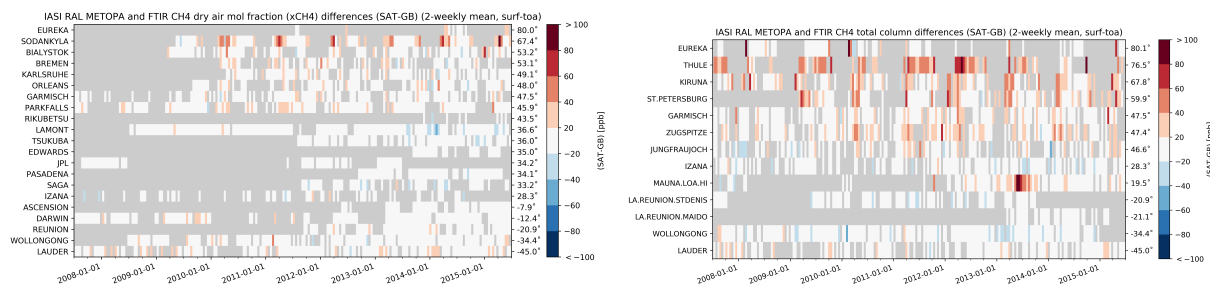
Figure 8. Mosaic plot of 2-weekly absolute mean differences (SAT-GB) at ground-based FTIR sites for the column averaged dry air mole fractions XCH$_4$ between RAL and ground-based FTIR measurements (left: TCCON; right: NDACC). The FTIR sites are sorted by their latitudes from north to south.
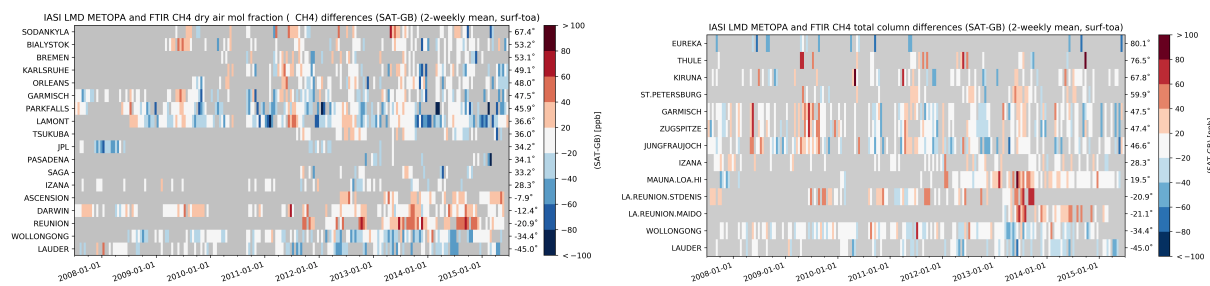
Figure 9. Same as Figure 8, but for mtCH$_4$ from LMD and ground-based FTIR measurements.
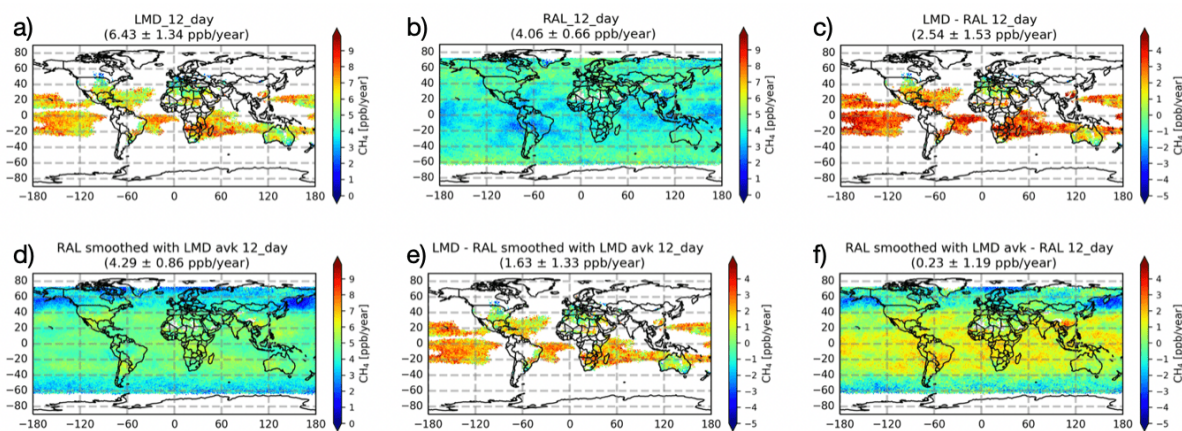
Figure 10. The mt(X)CH$_4$ annual growth derived from LMD (a), RAL (b) RAL_LMDavk (d) daytime measurements, together with their difference between LMD and RAL (c), between LMD and RAL_LMDavk (e), between RAL and RAL_LMDavk (f). The CH$_4$ annual growth calculated at the pixel where the missing values are less than 12 month between July 2007 and June 2015.
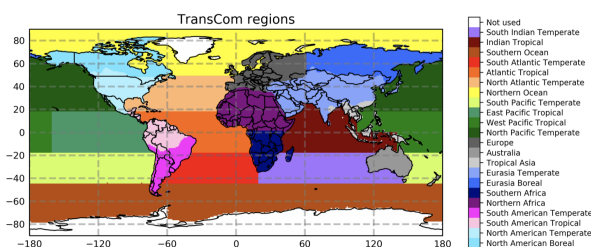
Figure 11. The TransCom map, including 11 land regions and 11 ocean regions.
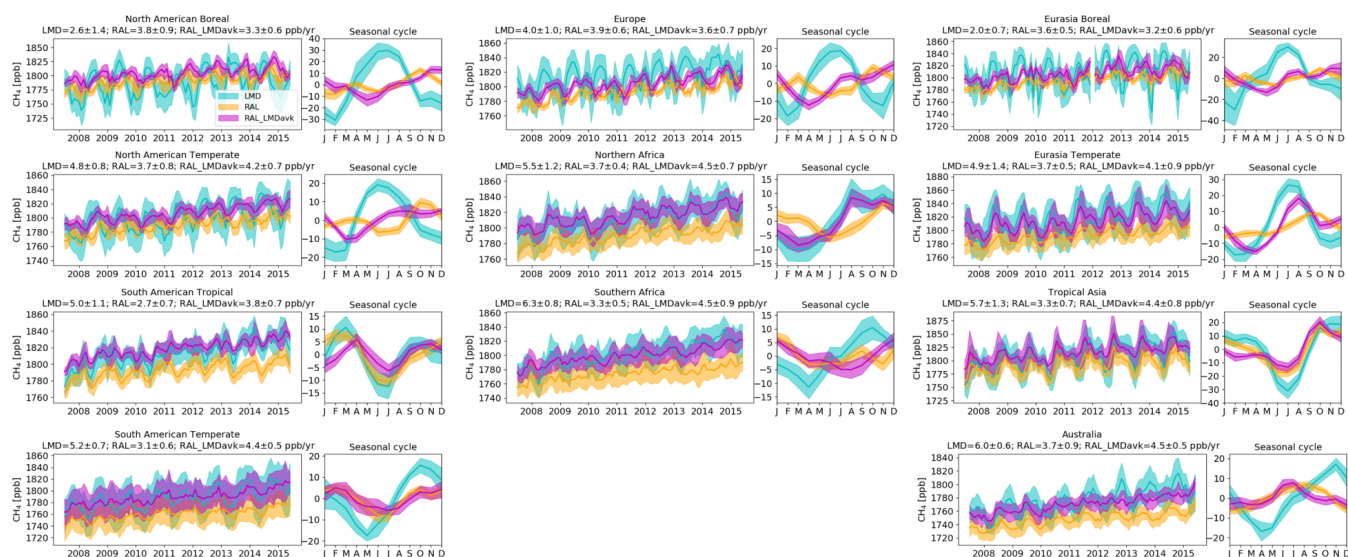
Figure 12. The time series of the LMD, RAL, and RAL_LMDavk CH_4 monthly means (solid lines) and standard deviations (shadow), together with the seasonal variations of CH_4 at 11 land TransCom regions.
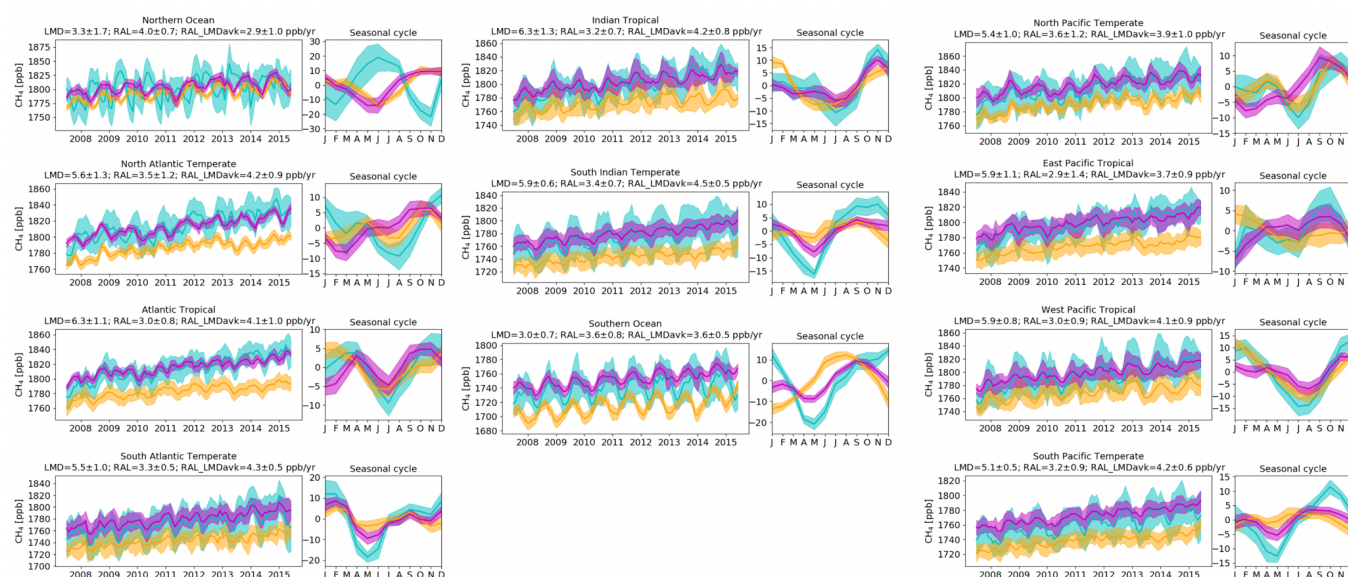
Figure 13. Same as Figure 12, but at 11 ocean TransCom regions.
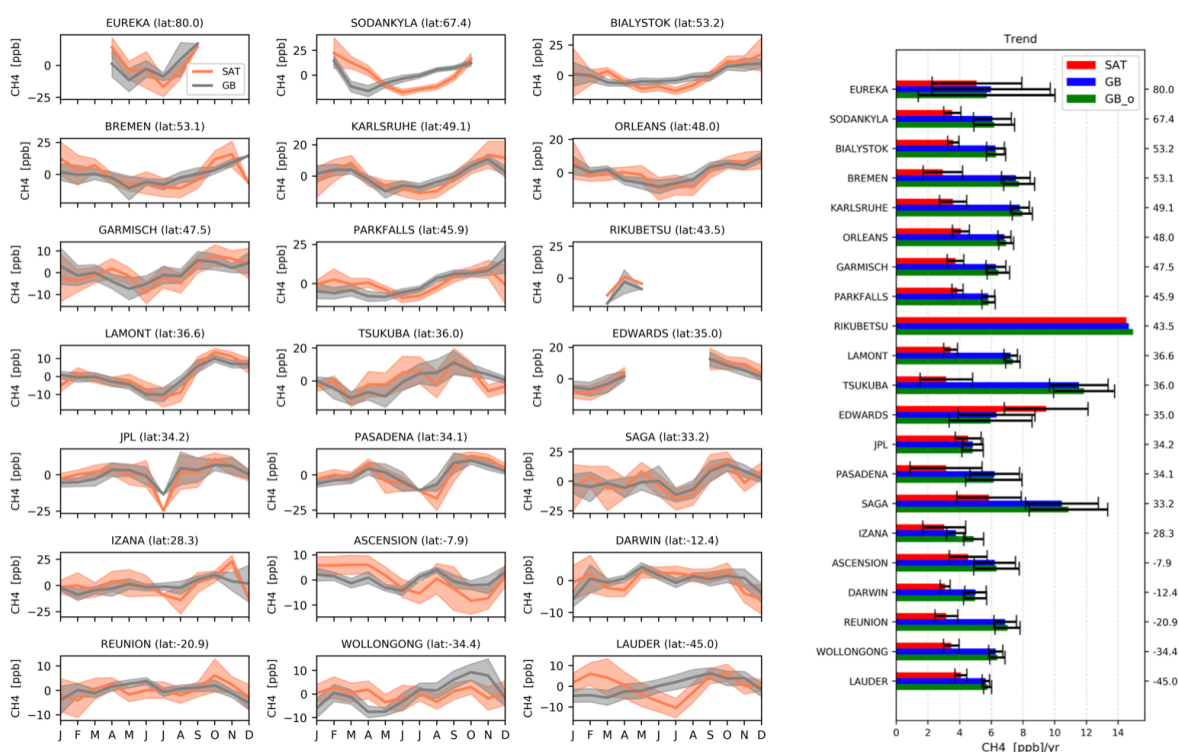
Figure 14. Left panels: the seasonal variations of XCH$_4$ observed by RAL (SAT) and smoothed TCCON (GB) measurements at each site. Right panel: the XCH$_4$ annual growths derived from RAL observations (SAT), TCCON measurements after smoothing (GB) and original TCCON measurements (GB_o). The latitude of the TCCON site is also remarked in the title or the y-axis.
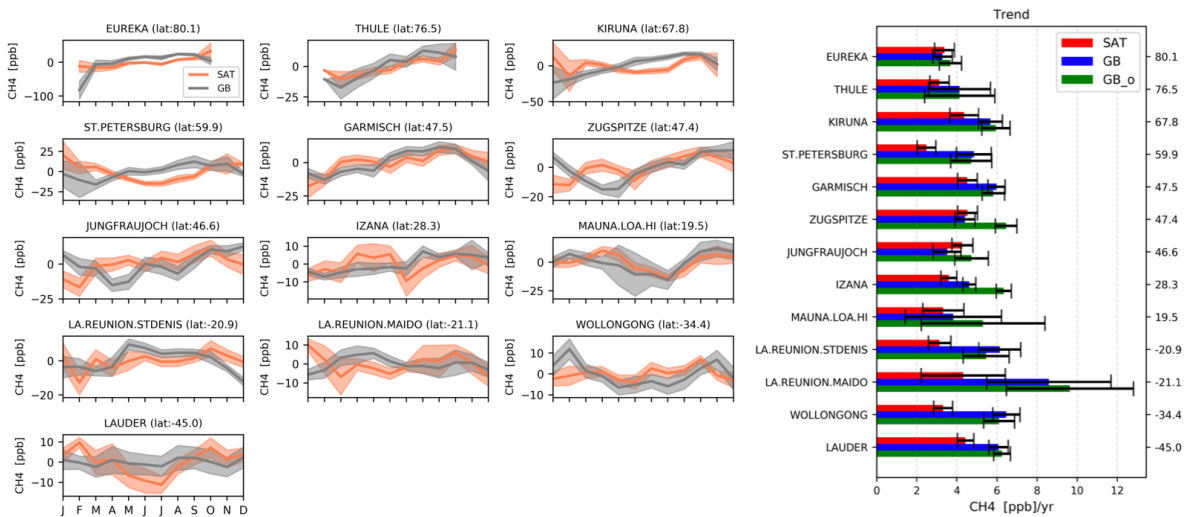
Figure 15. Same as Figure 14, but for RAL and NDACC measurements.
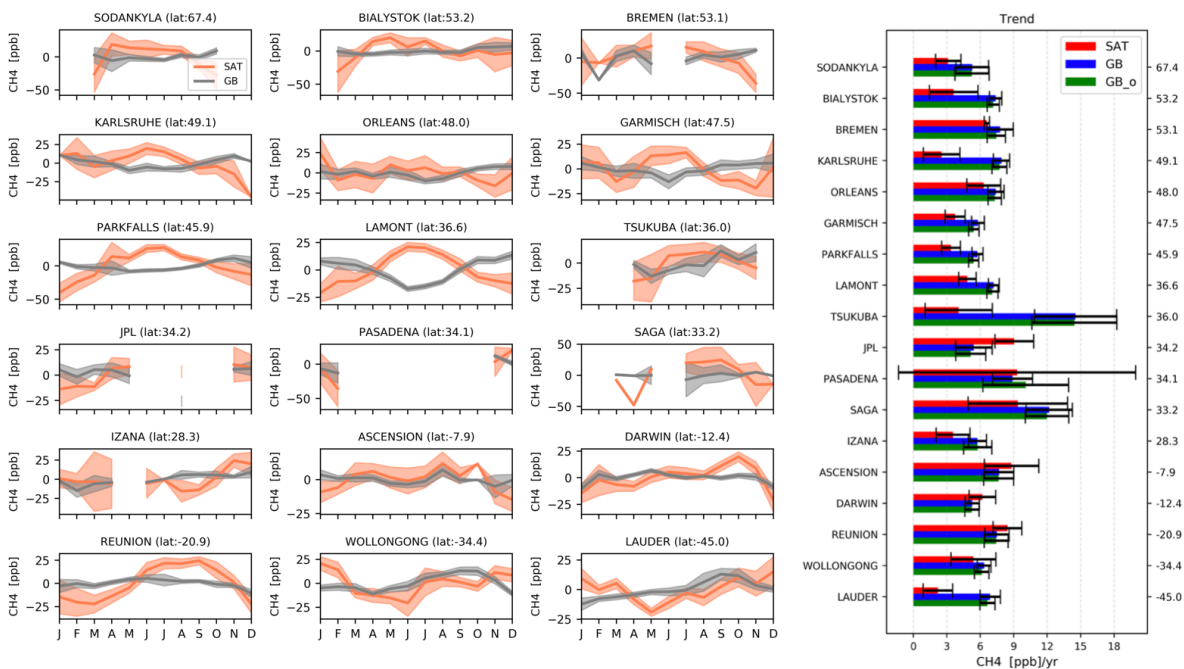
Figure 16. Same as Figure 14, but for LMD and TCCON measurements.
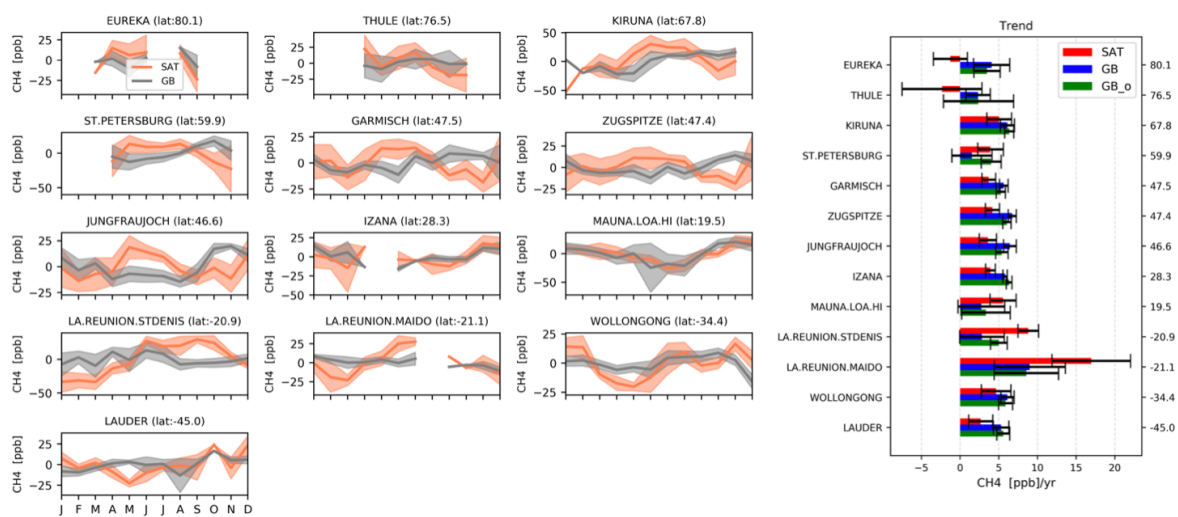
Figure 17. Same as Figure 14, but for LMD and NDACC measurements.
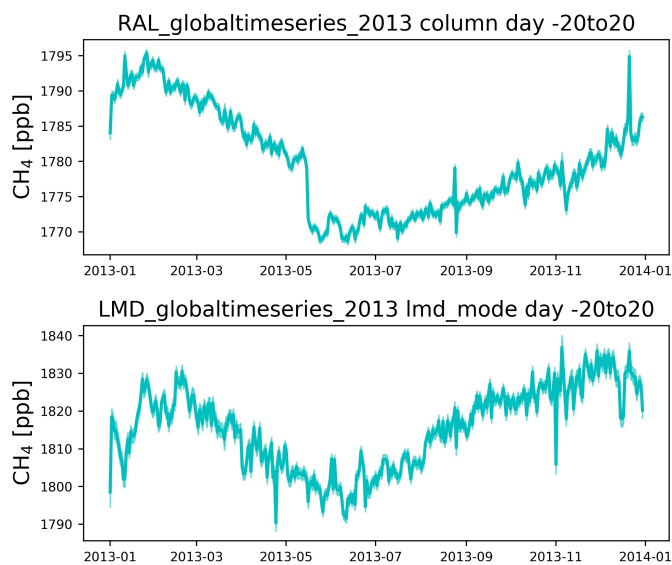
Figure 18. Evolution of the average CH$_4$ concentration around the 16th of May 2013, for the -20° to 20° latitude band for RAL (top) and LMD (bottom).
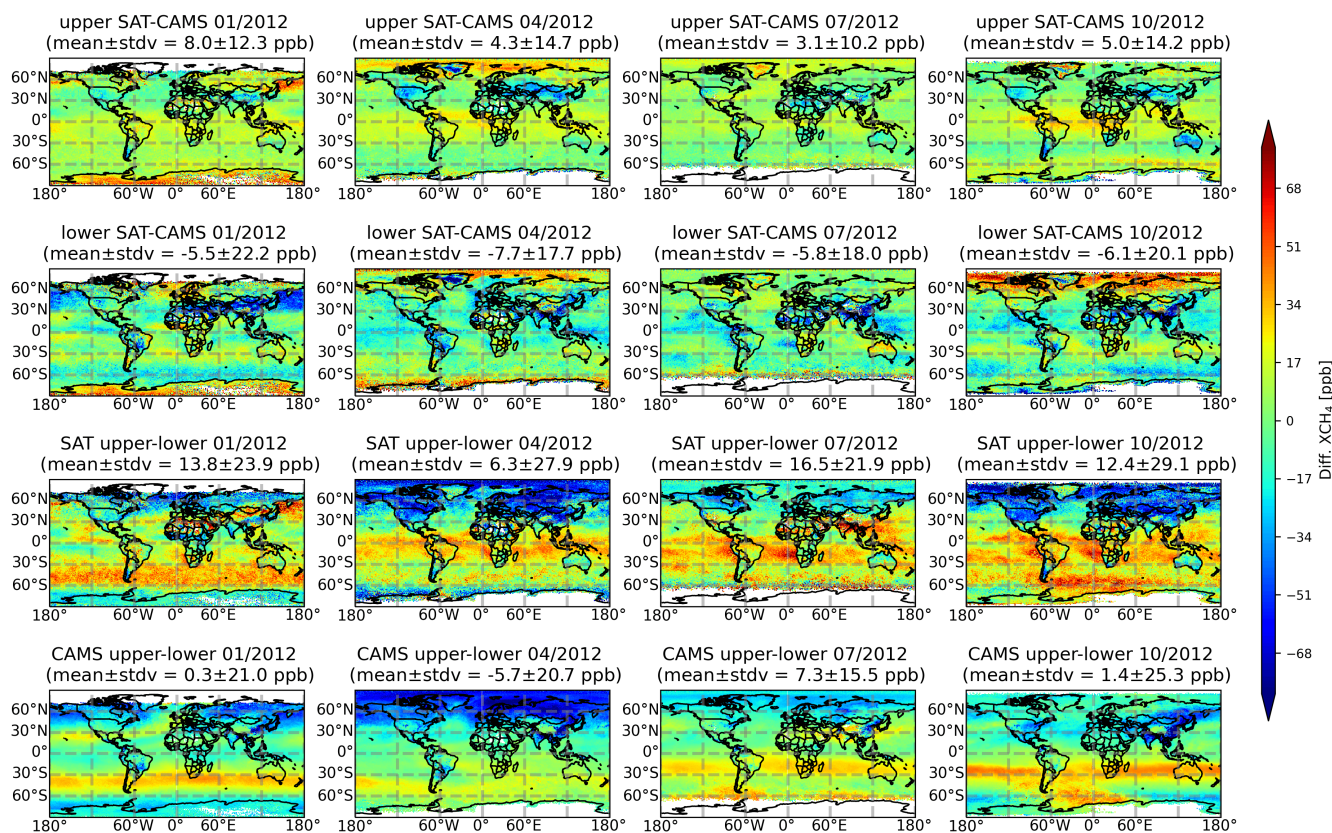
Figure 19. The difference of the qCH_4 in the upper layer (first row) and the lower layer (second row) between the RAL (SAT) and CAMS. Besides, the differences between the upper qCH_4 and lower qCH_4 derived from RAL (third row) and CAMS (last row) in January, April, July and October 2012.
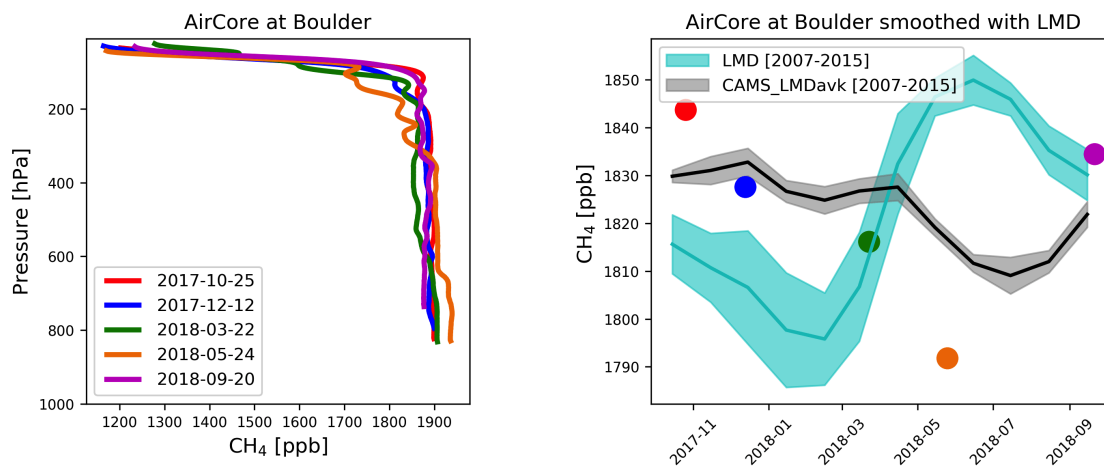
Figure 20. Left: the AirCore CH_4 profiles at Boulder between October 2017 and September 2018. Right: the time series of the $mtCH_4$ derived from the AirCore measurements with the smoothing correction using LMD weighting function, together with the $mtCH_4$ seasonal variation derived from LMD measurements between July 2007 and June 2015 with a constant shift using the mean of the 5 AirCore measurements.
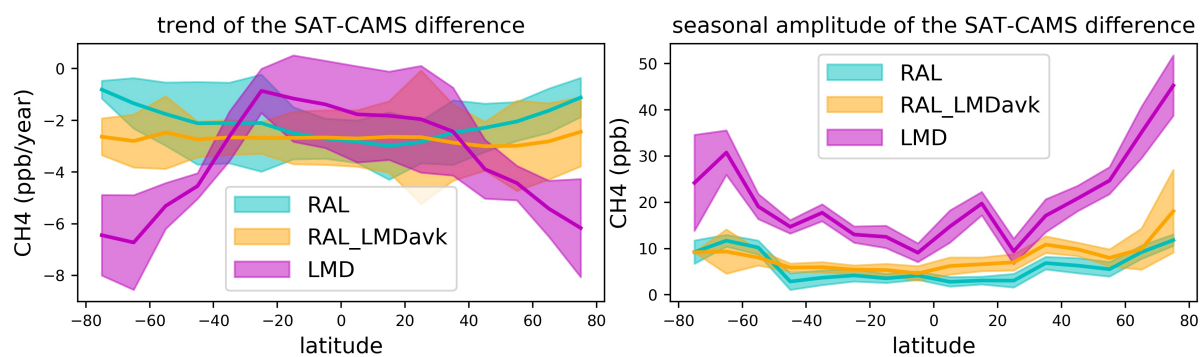

Figure 21. Left: long term trend values (ppb/year) for the satellite-CAMS residuals for $10°$ wide latitude bands. Right: the time series of the $mtCH_4$ derived from the AirCore measurements with the smoothing correction using LMD weighting function, together with the $mtCH_4$ seasonal variation derived from LMD measurements between July 2007 and June 2015 with a constant shift using the mean of the 5 AirCore measurements.